

1 **Future changes in African heatwaves and their drivers at the convective scale**

2 C. E. Birch¹, L. S. Jackson¹, D. L. Finney^{1,2}, J. M. Marsham³, R. A. Stratton⁴, S. Tucker⁴, S.
3 Chapman¹, C. A. Senior⁴, R. J. Keane^{1,4}, F. Guichard⁵, E. J. Kendon⁴

4 ¹School of Earth and Environment, University of Leeds, Leeds, UK

5 ²Ronin Institute for Independent Scholarship, Montclair, NJ, USA

6 ³University of Leeds Met Office Strategic (LUMOS) Research Group, School of Earth and
7 Environment, University of Leeds, UK

8 ⁴Met Office, Exeter, UK

9 ⁵CNRM, Université de Toulouse, Météo-France, CNRS, Toulouse, France

10 Corresponding author: Cathryn Birch, c.e.birch@leeds.ac.uk

11 For submission to Journal of Climate

12 **Word count:** 8850

13 **Key words** heat stress, heatwave, wet bulb, Africa, convective scale, climate change

14 **Abstract**

15 The future change in dry and humid heatwaves is assessed in 10 year pan-African convective
16 scale (4.5km) and parameterised convection (25km) climate model simulations. Compared to
17 reanalysis, the convective scale simulation is better able to represent humid heatwaves than
18 the parameterised simulation. Model performance for dry heatwaves is much more similar.
19 Both model configurations simulate large increases in the intensity, duration and frequency
20 of heatwaves by 2100 under RCP8.5. Present day conditions that occur on 3 to 6 heatwave
21 days per year will be normal by 2100, occurring on 150-180 days per year. The future change
22 in dry heatwaves is similar in both climate model configurations, whereas the future change
23 in humid heatwaves is 56% higher in intensity and 20% higher in frequency in the convective
24 scale model. Dry heatwaves are associated with low rainfall, reduced cloud, increased surface
25 shortwave heating and increased sensible heat flux. In contrast, humid heatwaves are
26 predominately controlled by increased humidity, rainfall, cloud, longwave heating and
27 evaporation, with dry bulb temperature gaining more significance in the most humid regions.
28 Approximately one third (32%) of humid heatwaves commence on wet days. Moist processes
29 are known to be better represented in convective scale models. Climate models with
30 parameterised convection, such as those in CMIP, may underestimate the future change in
31 humid heatwaves, which heightens the need for mitigation and adaptation strategies and
32 indicates there may be less time available to implement them to avoid future catastrophic
33 heat stress conditions than previously thought.

34 **Significance statement**

35 Temperatures are higher in dry heatwaves, but humid heatwaves can be more dangerous, as
36 the ability to cool by sweating is limited. We found that dry heatwaves are caused by
37 decreased cloud, allowing the sun to heat the surface, whereas humid heatwaves are caused
38 by increased cloud, rainfall and evaporation from the surface. We found that a state-of-the-
39 art very high resolution climate model predicts a larger future change in humid heatwaves
40 compared to a more traditional global climate model. Previous estimates of the prevalence
41 of humid heatwaves in the future may therefore be underestimated. If we do not cut
42 emissions of greenhouse gases, present-day heatwave conditions could be experienced on up
43 to half of all days of the year by 2100.

44 **1 Introduction**

45 There is mounting evidence that heatwaves, regardless of definition, have increased in
46 intensity, frequency and duration over Africa over the last three decades (Ceccherini et al.
47 2017; Fontaine et al. 2013; Lyon 2009; Moron et al. 2016; Seneviratne et al. 2021). The IPCC
48 Working Group 1 Sixth Assessment Report (Seneviratne et al. 2021) states that at the
49 continental scale, it is “very likely” the intensity and frequency of African hot extremes will
50 increase even under 1.5°C global warming, and the changes are “virtually certain” to occur
51 under 4°C global warming (Dosio 2017; Fitzpatrick et al. 2020a; Perkins-Kirkpatrick; Lewis
52 2020; Russo et al. 2016). Vicedo-Cabrera et al. (2021) attribute more than 40% of heat-related
53 mortality in South Africa during the period 1991-2018 to human-induced climate change.

54 Humid heatwaves are a combined measure of both temperature and humidity. Humidity
55 limits the body’s ability to sweat and therefore plays a major role in heat stress (i.e. when the
56 body’s ability to control its internal temperature starts to fail, Kjellstrom et al. (2016)).
57 Equatorial Africa, in particular, is projected to be a global hotspot for heat stress by the end
58 of the century (Coffel et al. 2017; Dosio et al. 2018; Mora et al. 2017). The impacts of heat
59 stress in Africa – including deaths - go largely unreported (Harrington; Otto 2020) and the
60 sparse observation network means humid temperature extremes in particular are hard to
61 detect. Despite this, a small number of studies have shown that heatwaves cause harm in
62 Africa (Azongo et al. 2012; Diboulo et al. 2012).

63 There is limited literature on the drivers of humid heatwaves anywhere in the world
64 (Raymond et al. 2021) and the vast majority of research on African heatwave drivers is
65 focused on dry-bulb heatwaves in the Sahel region of sub-Saharan Africa. Dry-bulb
66 temperature extremes in the Sahel due to moisture advection and surface longwave heating
67 through the water vapour greenhouse gas effect have been highlighted in a number of studies
68 (Fontaine et al. 2013; Guigma et al. 2020; Guigma et al. 2021; Llargeron et al. 2020; Oueslati
69 et al. 2017). Bouniol et al. (2021) analysed daily maximum dry-bulb temperature (daytime)
70 and daily minimum dry-bulb temperature (nighttime) heatwaves over the Sahel using satellite
71 derived cloud, aerosol, water vapour and radiative fluxes. They found that daytime heatwaves
72 occur during reduced cloud, a lower aerosol load and increase surface shortwave radiation
73 flux. Conversely, nighttime heatwaves occur during periods with increased cloud, aerosol,

74 water vapour and a resulting increase in longwave heating than exceeds the decrease in
75 shortwave heating.

76 Even within the discipline of meteorology, there is no universally accepted metric for dry or
77 humid heatwaves and different metrics do not necessarily identify the same events (Guigma
78 et al. 2020). A number of recent global studies have focused on metrics that account for both
79 temperature and humidity because both are physiologically important for human heat stress
80 (Coffel et al. 2017; Mora et al. 2017; Russo et al. 2017). Globally, 74% of the world's
81 population is projected to be exposed to deadly heat stress for at least 20 days per year by
82 2100 under RCP8.5 (Mora et al. 2017). South Asian wet-bulb temperature is projected to
83 approach, and in a few locations exceed, the critical threshold of 35°C, which is considered
84 the limit of human survivability, by 2100 under high emission scenarios (Im et al. 2017; Pal;
85 Eltahir 2016).

86 Projections of future heat extremes are almost ubiquitously provided by relatively coarse
87 resolution regional (Gutowski Jr et al. 2016) or global climate (Eyring et al. 2016; Taylor et al.
88 2012) models, which require a parameterisation scheme to represent convective rainfall
89 processes. Such models are known to poorly represent tropical rainfall characteristics,
90 whereas convective-scale climate models are better able to represent intense rainfall and dry
91 spells (Berthou et al. 2019b; Finney et al. 2020; Prein et al. 2015), related processes such as
92 storm lifecycles and propagation (Crook et al. 2019; Finney et al. 2020), the atmospheric
93 overturning circulation (Hart et al. 2018; Jackson et al. 2020), the atmospheric water cycle
94 (Birch et al. 2014b; Finney et al. 2019) and soil moisture-precipitation feedbacks (Taylor et al.
95 2013). Additionally, they project larger future increases in rainfall extremes (Berthou et al.
96 2019a; Finney et al. 2020; Kendon et al. 2014; Kendon et al. 2019). Emerging studies suggest
97 that heat extremes over Europe are better represented and the increases under climate
98 change are larger in magnitude in convective-scale climate models (Kennedy-Asser et al.
99 2020; Tölle et al. 2018). It is not currently known if African heat extremes are better
100 represented in convective-scale models, although given the crucial role of convection in
101 African weather, the representation of convection is likely to be important. It is, therefore,
102 critical to understand how African heatwave projections from global models are affected by
103 their parameterisation of convection.

104 This study uses 10-year pan-African climate simulations with 4.5km (convective-scale) and
105 25km (convection-parameterised) horizontal grid-spacing (Senior et al. 2021; Stratton et al.
106 2018). We evaluate the present day mean temperature and humidity in the climate models
107 using observations and reanalysis (Section 3.1). We assess the present-day values and future
108 changes (2100, RCP 8.5) in the intensity, duration and frequency of wet and dry bulb
109 heatwaves in the climate model simulations (Section 3.2). We demonstrate the contrasting
110 drivers of wet and dry bulb heatwaves over Africa (Section 3.3) and show how the drivers of
111 humid heatwaves differ over different regions of Africa (Section 3.4). We explain why the
112 convective-scale climate model simulates a larger number of more intense and longer
113 duration heatwaves under climate change than the climate model with parameterised
114 convection (Section 3.4).

115 **2 Data and Methods**

116 **2.1. Model simulations**

117 This study utilises two 10-year regional atmosphere-only climate simulations using the Met
118 Office Unified Model (MetUM) run over a pan-Africa domain of 25°W-57°E, 45°S-40°N
119 (Stratton et al. 2018). Both simulations are driven by the N512 (approximately 25km x 40km
120 in the tropics) global atmosphere-only (GA7) configuration of the MetUM (Walters et al.
121 2017). The first regional model (CP4) has a horizontal grid-spacing at the equator of 4.5 × 4.5
122 km (0.04° × 0.04°) and is ‘convective-scale’, i.e. its horizontal resolution is sufficient to not
123 require a parameterisation for convection and it is switched off. The second regional model
124 (P25) has a horizontal grid-spacing matching the global model and includes parameterised
125 convection (Gregory; Rowntree 1990; Walters et al. 2017). P25 is also based on the GA7
126 configuration, but in an attempt to restrict differences between P25 and CP4 to convection
127 some settings such as soil types and aerosol forcing have been made the same as those in
128 CP4.

129 In the historical period, representing the years 1997-2006, all models use Reynolds daily Sea
130 Surface Temperature (SST) observations (Reynolds et al. 2007; Stratton et al. 2018). The
131 future climate simulations use the Representative Concentration Pathway (RCP) 8.5 for
132 greenhouse gas concentrations for the year 2100 (Moss et al. 2010). In all the future
133 simulations (CP4FUT, P25FUT and the driving GCM) the average SST change between 1975–

134 2005 and 2085–2115 in a separate CMIP5 HadGEM2-ES RCP8.5 run is added to the historical
135 SSTs (Kendon et al. 2019).

136 The CP4 data was interpolated onto the P25 grid and all subsequent analysis is performed on
137 the P25 grid. Regridding the P25 and CP4 data onto a much coarser grid of $2^\circ \times 2^\circ$ made
138 negligible difference to the results (not shown). The full 10 years of simulation data, from
139 January 1997 to December 2006, was used. Dropping the first year to allow for spin-up made
140 negligible difference to all results (not shown).

141 **2.2. Observations and reanalysis**

142 We diagnose T_{\max} heatwaves using near-surface daily maximum temperature (T_{\max}) from the
143 Berkeley Earth Surface Temperature gridded dataset (BEST). It uses the statistical Kriging
144 method to interpolate data from weather stations compiled from a number of data archives
145 onto a global regular $1^\circ \times 1^\circ$ grid (Rohde; Hausfather 2020). We evaluate the mean
146 temperature in the climate models using monthly mean near-surface temperature from the
147 Climatic Research Unit (CRU) TS4.03 reference dataset, on a $0.5^\circ \times 0.5^\circ$ grid (Harris et al. 2020).

148 We diagnose heatwaves using hourly data from the fifth generation of the European
149 reanalysis (ERA5) at the native horizontal resolution of $0.25^\circ \times 0.25^\circ$ ($\sim 30\text{km}$) (Hersbach et al.
150 2020). We note that ERA5 is produced by an atmospheric model, itself with parameterised
151 convection. It cannot be considered as ‘observations’ and the drivers of the heatwaves in
152 ERA5 may suffer from similar biases as the climate models, particularly P25. Previous work
153 has compared and evaluated daily maximum and minimum dry bulb temperature in four
154 reanalysis products, including ERA-Interim, the ERA5 predecessor, against the BEST dataset
155 and found ERA-Interim performed the best (Barbier et al. 2018). There are limitations in using
156 reanalysis datasets but there are also likely big uncertainties in the BEST and CRU datasets
157 due to the sparsity of surface station observations over Africa.

158 There is no pan-African gridded observational dataset that resolves both the diurnal cycles in
159 near-surface temperature and humidity. Instead, to evaluate the diurnal cycles of dry and wet
160 bulb temperature and humidity in reanalysis and the climate model simulations, we use
161 hourly observations from three weather stations, with multiyear sub-hourly records that
162 include humidity. The first is in Skukuza, South Africa (-25.0°N , 31.5°E), which has data
163 available 2000-2013 (Pastorello et al. 2020), the second is in Demokeya, Kordofan, central

164 Sudan (13.3°N, 30.5°E), which has data available 2002-2012 (Ardö 2013) and the third is in
165 Banizoumbou, Niamey, Niger (13.5°N, 2.7°E), where data from 2008-2015 was used (Lebel et
166 al. 2009).

167 We use the daily Integrated Multi-satellitE Retrievals (IMERG) for Global Precipitation
168 Measurement (GPM) satellite retrievals of rainfall (Huffman 2014), available from mid-2000
169 to near-present. The IMERG data is interpolated onto the ERA5 grid before any analysis is
170 performed.

171 **2.3. Heatwave identification**

172 Heatwaves are defined using near-surface daily maximum dry (T_{\max}) or wet (T_{wbmax}) bulb
173 temperature over the pan-Africa region of 22°W-54°E, 42°S-37°N, which includes the Arabian
174 Peninsula, for land points only. This means a 3° band around the edge of the model domains
175 have been removed to allow for the effects of the lateral boundary conditions. There are
176 various quantities that can be used to represent humidity in heat stress, including wet-bulb
177 temperature, wet bulb globe temperature and apparent temperature. Sherwood (2018)
178 shows that although all three of these quantities increase with increasing humidity, wet bulb
179 temperature is the most sensitive to humidity, which makes it a good choice here in order to
180 best highlight the differences in the drivers of T_{\max} and T_{wbmax} heatwaves.

181 Hourly wet-bulb temperature is computed from hourly specific humidity, dry bulb
182 temperature and pressure using the method of Davies-Jones (2008) and then the daily
183 maximum, T_{wbmax} , is found. The results are not sensitive to using hourly dry-bulb temperature
184 to compute T_{\max} , rather than the daily dry-bulb maximum temperature output directly from
185 the model simulations. For T_{wbmax} , it was necessary to compute the daily maximums from the
186 hourly data because, due to the diurnal cycle of humidity, it is essential to use hourly, rather
187 than daily mean, humidity data to compute T_{wbmax} (see Section 2.4). For consistency, we also
188 use hourly data to calculate T_{\max} .

189 Heatwaves were identified as follows (described here for T_{wbmax} heatwaves; a description of
190 the differences between how T_{wbmax} and T_{\max} heatwaves are diagnosed follows):

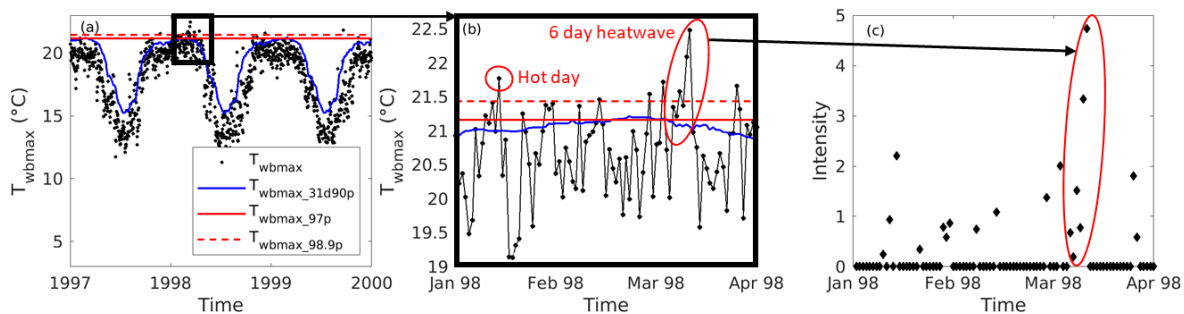
- 191 1. For each gridbox, the 90th percentile of T_{wbmax} over a 31-day running window,
192 $T_{\text{wbmax_31d90p}}$ (blue line, Figure 1) and the 97th percentile of daily maximum wet bulb

193 temperature over all days in the dataset, T_{wbmax_97p} (red solid line, Figure 1) are
 194 computed.

195 2. Hot days are defined as days where T_{wbmax} (black dots, Figure 1) are above both the
 196 blue and red solid lines, i.e. unseasonably warm days in the colder months are not
 197 diagnosed as hot days.

198 3. A heatwave event is defined as 3 or more consecutive hot days. A “heatwave day” is
 199 defined as each individual day within a heatwave event.

200 Three key metrics are recorded for each gridbox: the duration of each heatwave, the intensity
 201 of each heatwave day (defined below) and the total number of heatwave days that occur over
 202 the length of the dataset, i.e. the frequency. The total number of heatwave days is analysed,
 203 rather than the number of heatwave events, because the future change in heatwaves in the
 204 climate models is so large that most days in the future are diagnosed as heatwaves, so the
 205 number of events can decrease whilst the number of heatwaves days increases, and so
 206 analysing the number of heatwave events (and the heatwave duration) is mis-leading.



207
 208 **Figure 1** Illustration of the heatwave identification method for one arbitrary gridbox in CP4.
 209 (b) and (c) are consecutively zoomed in views of (a). The black dots represent daily T_{wbmax} over
 210 an example 3 year time slice. The blue line is the 90th percentile of T_{wbmax} over a 31-day running
 211 window. The red solid and dashed lines are the 97th and 98.9th percentiles respectively of
 212 T_{wbmax} over all days and all years. The dots in (c) show the unit-less heat intensity on each
 213 identified hot day.

214
 215 The intensity of each heatwave day is computed using a modified version of Equation 2 in
 216 Russo et al. (2015):

217

$$I = \frac{T_{wbmax} - T_{wbmax_97p}}{T_{wbmax_98.9p} - T_{wbmax_97p}}$$

218 where $T_{wbmax_98.9p}$ is the 98.9th percentile of daily maximum wet bulb temperature over all
219 days in the dataset (red dashed line, Figure 1). I is a dimensionless measure of the intensity
220 of each heatwave day relative to the variability of the hottest days that occur in each grid box.

221 This heatwave methodology was chosen because: (1) it is a percentile-based metric, which
222 allows ERA5 and the climate models to be directly compared regardless of differences in their
223 mean climatology of temperature and humidity, (2) it is computed for each gridbox
224 separately, which allows the widely varying climates in Africa to be directly compared, and (3)
225 it is possible to look at the intensity, duration and frequency of heatwaves as separate
226 metrics.

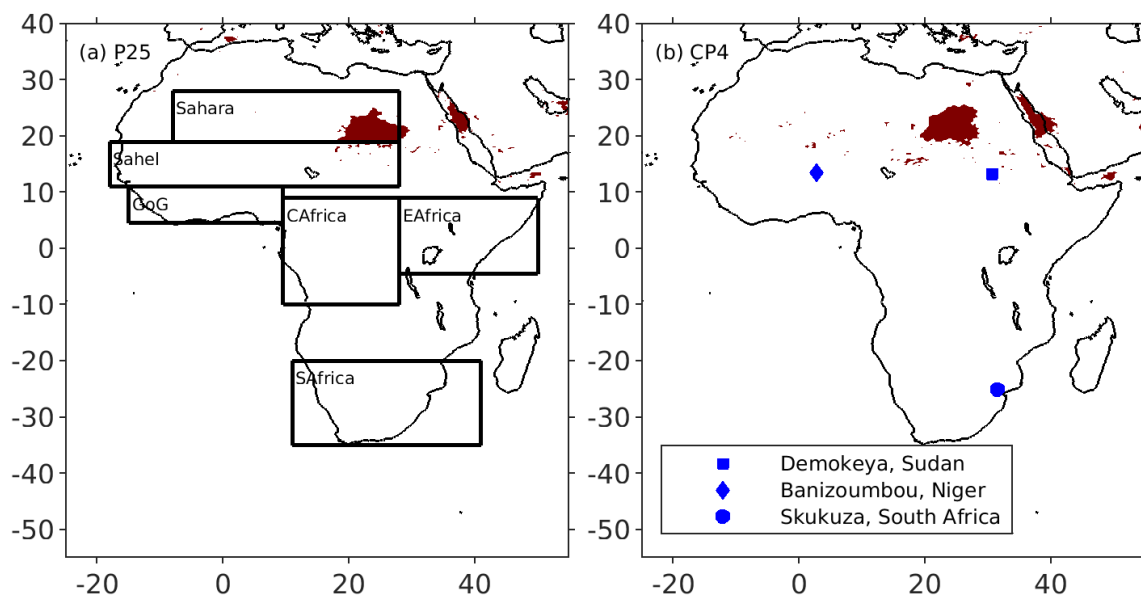
227 Heatwaves in CP4FUT and P25FUT are computed twice: once relative to the present-day
228 baseline (i.e. T_{wbmax_31d90p} , T_{wbmax_97} and $T_{wbmax_98.9p}$ are taken from the present day simulation
229 at each gridbox) and once relative to the future climate baseline (i.e. T_{wbmax_31d90p} , T_{wbmax_97}
230 and $T_{wbmax_98.9p}$ are taken from the future climate simulation at each gridbox). Heatwaves
231 computed using the present-day baseline are used throughout the paper, except in Figures
232 13, 15 and 16, where the future change in heatwave drivers is assessed. Future heatwaves
233 are so frequent and long in duration under climate change that identifiable individual
234 heatwaves do not exist in the future. Therefore, using the future climate baseline diagnoses
235 a similar number of discrete heatwaves as are diagnosed in the present day.

236 Dry-bulb heatwaves are computed in the same way as above, by replacing T_{wbmax} with T_{max} .
237 The only other difference is that the two percentile thresholds (red solid and dashed lines in
238 Figure 1) are set at T_{max_98} and $T_{max_99.9p}$ for dry-bulb heatwaves, rather than the 97th and 98.9th
239 percentile used for T_{max} . There is no clear choice of percentile in the literature, with different
240 authors choosing to use different values (Guigma et al. 2020; Lyon 2009; Raymond et al. 2021;
241 Russo et al. 2015). The consequence of using different percentiles for T_{max} and T_{wbmax}
242 heatwaves is that the values of intensity are not directly comparable. However, it is done to
243 make the number of T_{max} and T_{wbmax} heatwaves diagnosed in the present day similar, to
244 provide consistency for the heatwave driver analysis.

245 For ERA5 we use two periods: (1) 1997-2006 for comparison of the ERA5 heatwave metrics to
246 the present day climate simulations and (2) 2000-2019 when looking at atmospheric
247 heatwave drivers, in order to align with the availability of the GPM rainfall observations. Here,

248 we also compare with the period 1987-2016 to assess the impact of using a longer timeseries
 249 on the heatwave metrics. The mean and standard error of the pan-African heatwave metrics
 250 in ERA5 over 1997-2006, 1987-2016 and 2001-2019 are intensity: 1.36 ± 0.002 , 1.41 ± 0.002 ,
 251 1.50 ± 0.002 , duration: 3.93 ± 0.003 , 4.01 ± 0.002 , 3.97 ± 0.002 days and frequency: 2.5 ± 0.05 ,
 252 2.7 ± 0.16 , 2.5 ± 0.10 days per year respectively. These are negligible differences apart from in
 253 intensity, where a small climate change signal of higher intensity in later years is apparent,
 254 consistent with previous studies (Ceccherini et al. 2017). The relative importance of the
 255 different heatwave drivers is not dependent on the period used (not shown).

256 Figure 2 illustrates the resulting T_{wbmax} heatwave diagnosis in P25 and CP4 for an example day.
 257 The methodology is able to identify large, spatially coherent heatwaves. 25 June 2001 is more
 258 than 4 years into the climate simulation, so the fact that both climate models produce a
 259 heatwave of a similar size and location at the same time, suggest that the lateral boundary
 260 conditions and SSTs (which are the same in both simulations) have a strong control on this
 261 event.



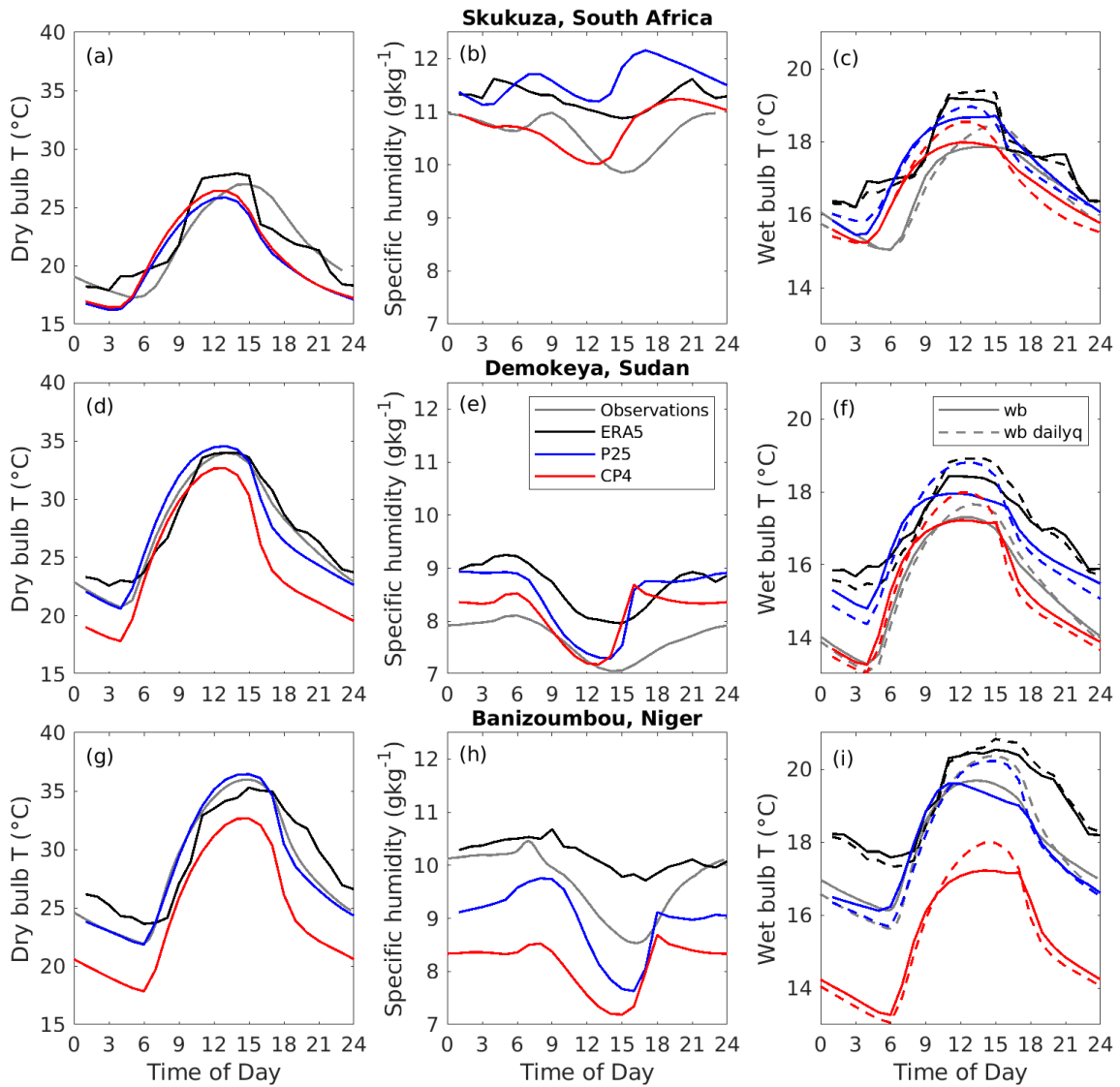
262
 263 **Figure 2** Example heatwave on 25 June 2001 in P25 and CP4. The gridboxes where a heatwave
 264 was identified on this day are marked in red. Also shown are the sub regions used later in the
 265 analysis and the locations of the three weather stations used in Figure 3. GoG = Gulf of Guinea.

266

267 **2.4. Daily vs. hourly specific humidity values in T_{wbmax} calculation**

268 The mean diurnal cycle of near-surface specific humidity and wet and dry bulb temperature
269 from ERA5, P25 and CP4 are plotted against observations from the three automatic weather
270 stations (Figure 3). Specific humidity has a diurnal cycle that is out of phase with the diurnal
271 cycle in dry-bulb temperature at both locations, which is consistent with dry-air entrainment
272 into the boundary layer during the day and moisture advection at night (Couvreur et al. 2015).
273 This has a strong control on the magnitude and timing of T_{wbmax} , causing a flattening of the
274 diurnal peak of wet bulb temperature (solid lines, Figure 3c,f,i).

275 Due to the lack of availability of sub-daily humidity diagnostics from ensemble model studies
276 such as CMIP5 (Taylor et al. 2012), CMIP6 (Eyring et al. 2016) and CORDEX (Gutowski Jr et al.
277 2016), past studies that diagnose humid heatwaves using the daily maximum wet bulb (or wet
278 bulb globe, WBGT) temperature (e.g. Russo et al. (2017) and Coffel et al. (2017)) necessarily
279 use the daily mean, minimum or maximum humidity to compute daily maximum humid-heat
280 metrics. Using daily mean specific humidity in the calculation of T_{wbmax} produces a smooth
281 diurnal cycle in wet-bulb temperature, which follows the shape of the diurnal cycle of dry bulb
282 temperature (dashed lines, Figure 3c,f,i). The impact of the choice of daily or sub-daily specific
283 humidity on the present-day heatwave metrics used in this study is strikingly large and
284 perhaps unpredictable, with no clear trend in the direction of the impact in ERA5, CP4 and
285 P25 (Figure S1). The future change in wet-bulb heatwave intensity, duration and frequency
286 are overestimated in both CP4 (by 106, 40 and 16% respectively) and P25 (by 73, 16 and 3%
287 respectively) when daily specific humidity is used in the T_{wbmax} calculation (Figure S1). This is
288 particularly important for wet-bulb temperature, which is the most sensitive to humidity out
289 of the most frequently used humidity-temperature indices (Sherwood 2018).



290

291 **Figure 3** Mean diurnal cycle of near-surface dry bulb temperature (left), near-surface specific
 292 humidity (middle) and wet bulb temperature (right) at the locations of the surface stations in
 293 South Africa (top), Sudan (middle) and Niger (bottom). Wet-bulb temperature is computed
 294 using both hourly and daily mean q . Using daily mean or hourly surface pressure has negligible
 295 impact on the wet-bulb calculation. The locations of the three stations are illustrated in Figure
 296 2.

297

298 2.5. Computation of anomalies and climatologies

299 Data in Figures 10, 14, 15 and 16 are presented as mean anomalies relative to a locally and
 300 temporally relevant climatology. For each heatwave diagnosed in ERA5 and the model
 301 simulations, a daily mean timeseries of each variable is extracted for a 31 day period, from
 302 day -15 to day +15, where day 0 is the onset of the heatwave. The local (i.e. gridbox specific)

303 daily mean annual cycle (31 values), smoothed using a 50-day running window, is subtracted
304 from each 31-day timeseries to produce anomalies from the mean climatology at the relevant
305 time of year. The bars in Figures 10, 14, 15 and 16 are an average of each anomaly over the
306 first 3 days of all diagnosed heatwaves, so that each heatwave is weighted equally in the
307 analysis. The exception is the humidity and temperature advection (q_{adv} , T_{adv}) in Figures 10
308 and 14, which are presented as absolute values for ease of interpretation.

309 **2.6. Statistical testing of rainfall distribution**

310 The Wilcoxon matched-pairs signed rank test is used to assess whether the distribution of
311 daily rainfall accumulations on heatwave days is statistically significantly different ($p < 0.01$) to
312 the climatological distribution of rainfall. For each heatwave, taking $d-5$ to $d5$ in turn (where
313 the first day of the heatwave is $d0$), the difference between the rainfall accumulation on d_x
314 and the rainfall accumulation on $d-15$ is computed, where $d-15$ is far enough away in time
315 from the heatwave event to be sufficiently independent. The Wilcoxon signed rank test is
316 performed 10,000 times on 1000 randomly selected difference-pairs for each day from $d-5$ to
317 $d5$. This process is then repeated using daily rainfall accumulation on $d+15$, to allow for
318 seasonal changes in rainfall between $d-15$ and $d+15$, which can be large around the time of
319 monsoon onset.

320 The Wilcoxon matched-pairs signed rank test determines whether two dependent samples
321 were selected from populations having the same distribution i.e. the null hypothesis is that
322 the medians of the heatwave and climatological rainfall are equal. It is an appropriate test
323 because rainfall data does not have a normal distribution, rather there are many more dry
324 and/or low rainfall days than wet days.

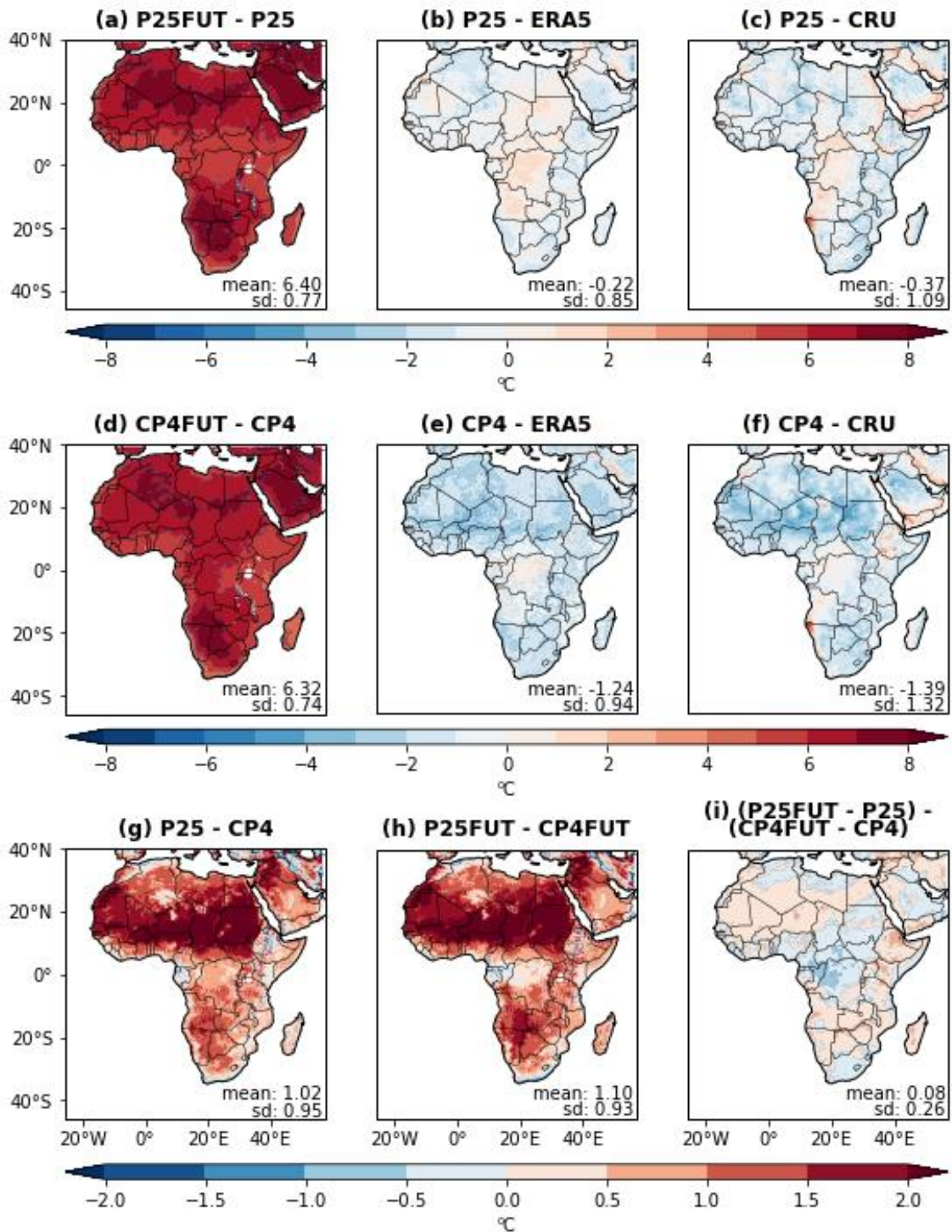
325 **3 Results**

326 **3.1 Annual mean temperature and humidity**

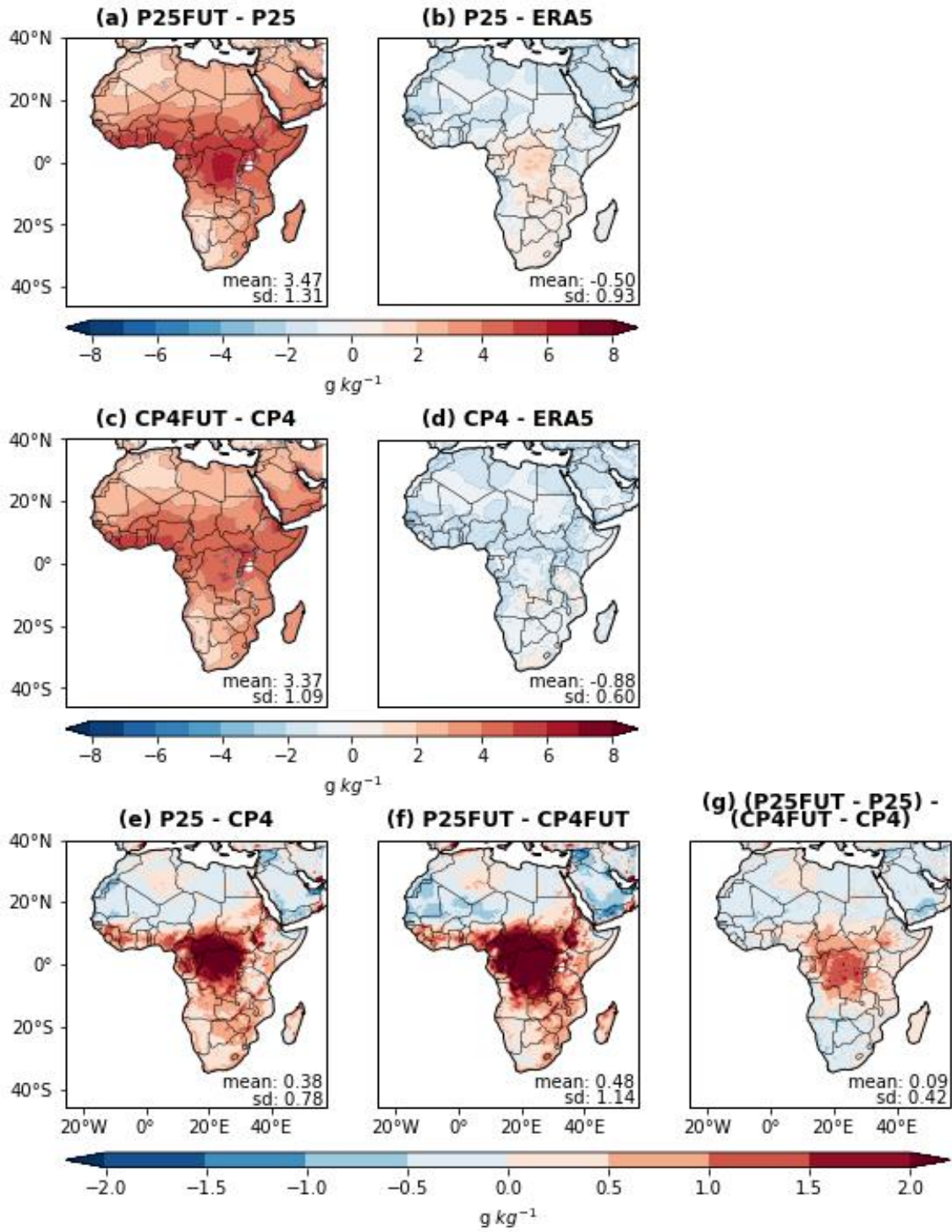
327 An assessment of the mean dry bulb temperature shows that there is a cold bias of 1.24 and
328 1.39°C in mean near-surface dry bulb temperature in CP4 compared to ERA5 and CRU
329 respectively (Figure 4e,f). P25 is also biased cold, but only by 0.22 and 0.37°C respectively
330 (Figure 4b,c). In both the present day and future climate, CP4 is on average $\sim 1^\circ\text{C}$ cooler than
331 P25 (Figure 4g,h). CP4 and P25 simulate future mean temperature increases by 2100 of 6.3

332 and 6.4°C respectively (Figure 4a,d), with P25 projecting a smaller increase in Central Africa
333 and CP4 predominately projecting a smaller increase elsewhere (Figure 3i).

334 Compared to ERA5, CP4 and P25 have a mean dry bias of 0.88 and 0.50 g/kg in specific
335 humidity respectively, although P25 is wetter by 1-2 g/kg over Central Africa (Figure 5b,d).
336 Both CP4 and P25 project mean future increases in specific humidity of ~3.4 g/kg (Figure 5a,c)
337 but the future change is ~1.5 g/kg larger in P25 over Central Africa and ~0.5 g/kg larger in CP4
338 elsewhere (Figure 5g). The resulting impact on mean wet-bulb temperature is a cold bias
339 relative to ERA5 of 1.1 and 0.5°C in CP4 and P25 respectively (Figure 6b,d), although the
340 humidity bias in P25 in Central Africa produces a warm bias in wet-bulb temperature of 0.5-
341 1°C. P25 is on average 0.6-0.7 °C warmer than CP4 in wet-bulb temperature in both the
342 present day and future, with a large region of central Africa being up to 2 °C warmer (Figure
343 6e,f). The future change in mean wet-bulb temperature is ~4.4°C in both CP4 and P25 (Figure
344 6a,c), with spatially variable differences in the future change between P25 and CP4 that are
345 fairly small due to the compensating effects of humidity and temperature biases in the
346 calculation of wet bulb temperature (Figure 6g). The cold and dry biases are consistent with
347 those in other climate models (Fischer; Knutti 2013; Zhao et al. 2015).

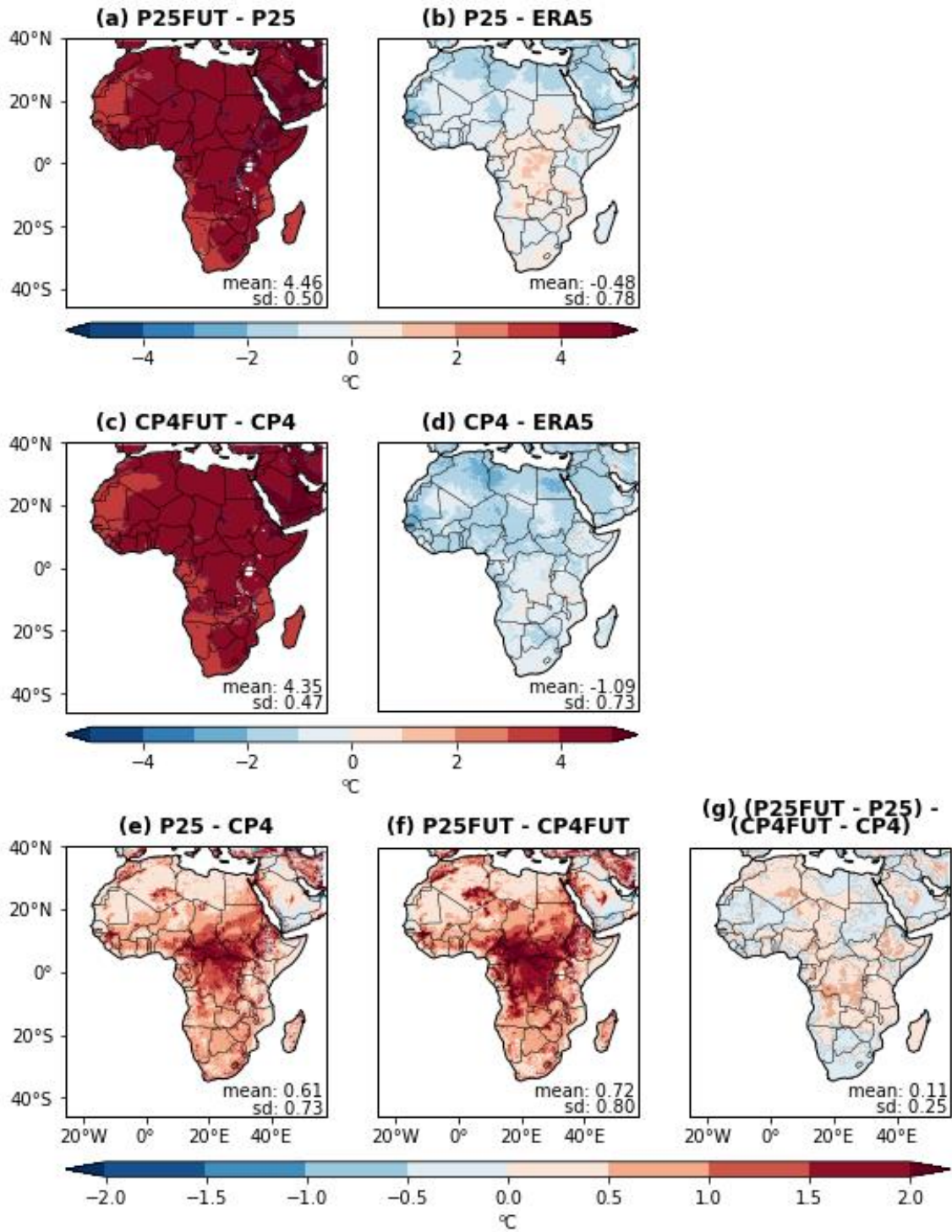


348
 349 **Figure 4** Mean near-surface dry-bulb temperature. (a,d) mean future changes, (b,e) difference
 350 between present-day model simulations and ERA5, (c,f) difference between present-day
 351 model simulations and CRU, (g,h,i) differences between P25 and CP4 in the present-day,
 352 future and the future change.



353

354 **Figure 5** Mean near-surface specific humidity. (a,d) mean future changes, (b,d) difference
 355 between present-day model simulations and ERA5, (e,f,g) differences between P25 and CP4
 356 in the present-day, future and the future change.



357

358 **Figure 6** Mean near-surface wet bulb temperature. (a,d) mean future changes, (b,d)
 359 difference between present-day model simulations and ERA5, (e,f,g) differences between P25
 360 and CP4 in the present-day, future and the future change.

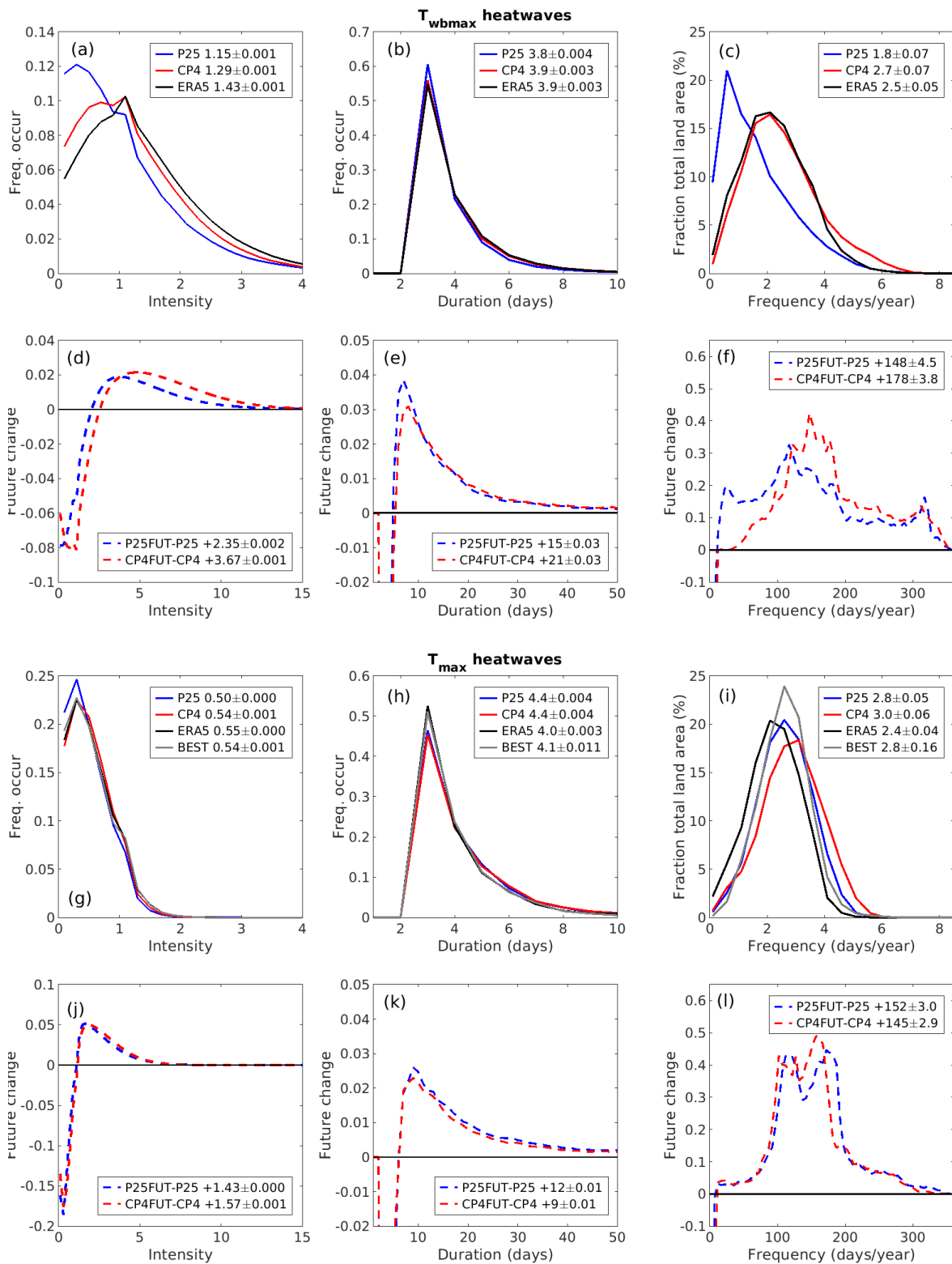
361 3.2 Wet and dry bulb heatwave metrics

362 Summaries of present day and the future change in intensity, duration and frequency of T_{wbmax}
363 and T_{max} heatwaves in ERA5, P25 and CP4 (and BEST for T_{max}) are shown in Figure 7. For T_{max}
364 intensity, there is relatively good agreement between ERA5, BEST and both climate models
365 (Figure 7g). For T_{wbmax} intensity, both CP4 and P25 are skewed towards intensities <1 ,
366 although CP4 much less so and is, therefore, in much better agreement with ERA5 (Figure 7a).
367 There is good agreement between P25, CP4 and ERA5 (and BEST for T_{max} heatwaves) for both
368 T_{wbmax} and T_{max} heatwave duration, with present day mean heatwave lengths of ~ 4 days
369 (Figure 7b,h). For frequency, there is reasonable agreement between the climate models and
370 observations for T_{max} heatwaves, with on average 2.4-3.0 days/yr (Figure 7i). For wet bulb
371 heatwaves, the distribution of heatwave frequency in P25 is skewed towards lower values,
372 with a mean in P25 of 1.8 days/yr compared with values of 2.7 days/yr and 2.5 days/yr in CP4
373 and ERA5 respectively (Figure 7c).

374 By 2100, under RCP8.5 both CP4 and P25 simulate large increases in all three metrics for both
375 T_{wbmax} and T_{max} heatwaves. Considering both types of heatwaves and both model simulations,
376 the ranges of future increases are +1.5 to +3.7 for intensity, +9 to +21 days for length, and
377 +145 to +178 days/yr for frequency (Figure 7d-f and j-l). The frequency increase can be
378 interpreted as, on average over all of Africa, up to half of all days of the year will experience
379 heat and/or humidity conditions that currently only occur on the annual hottest/most humid
380 2 to 3 days. With such large increases, the future heatwave duration metric becomes
381 inappropriate and the focus should be on the total number of heatwave days per year (i.e.
382 the frequency) and the intensity.

383 For T_{wbmax} heatwaves, the future change in intensity is 56% higher in CP4 than in P25 (Figure
384 7d) and the future change in frequency is 20% higher in CP4 than P25 (Figure 7f). For T_{max}
385 heatwaves the future change in intensity is only 10% higher in CP4 than P25 (Figure 7j) and
386 the future change in frequency is actually 5% higher in P25 than CP4 (Figure 7l). The model
387 differences and future changes are broadly similar in all six of the sub regions illustrated in
388 Figure 2 (not shown). Clearly there is much more disagreement between CP4 and P25 in the
389 future change of T_{wbmax} heatwaves than T_{max} heatwaves. Processes such as moisture
390 transport, cloud, evaporation and rainfall are potentially key drivers of humid heatwaves, and
391 it is known from previous work that moist processes are generally better represented in

392 convective-scale models than models with parameterised convection (Finney et al. 2020;
 393 Finney et al. 2019; Jackson et al. 2020; Kendon et al. 2019). The following section diagnoses
 394 and compares the drivers of T_{wbmax} and T_{max} heatwaves over the African continent.



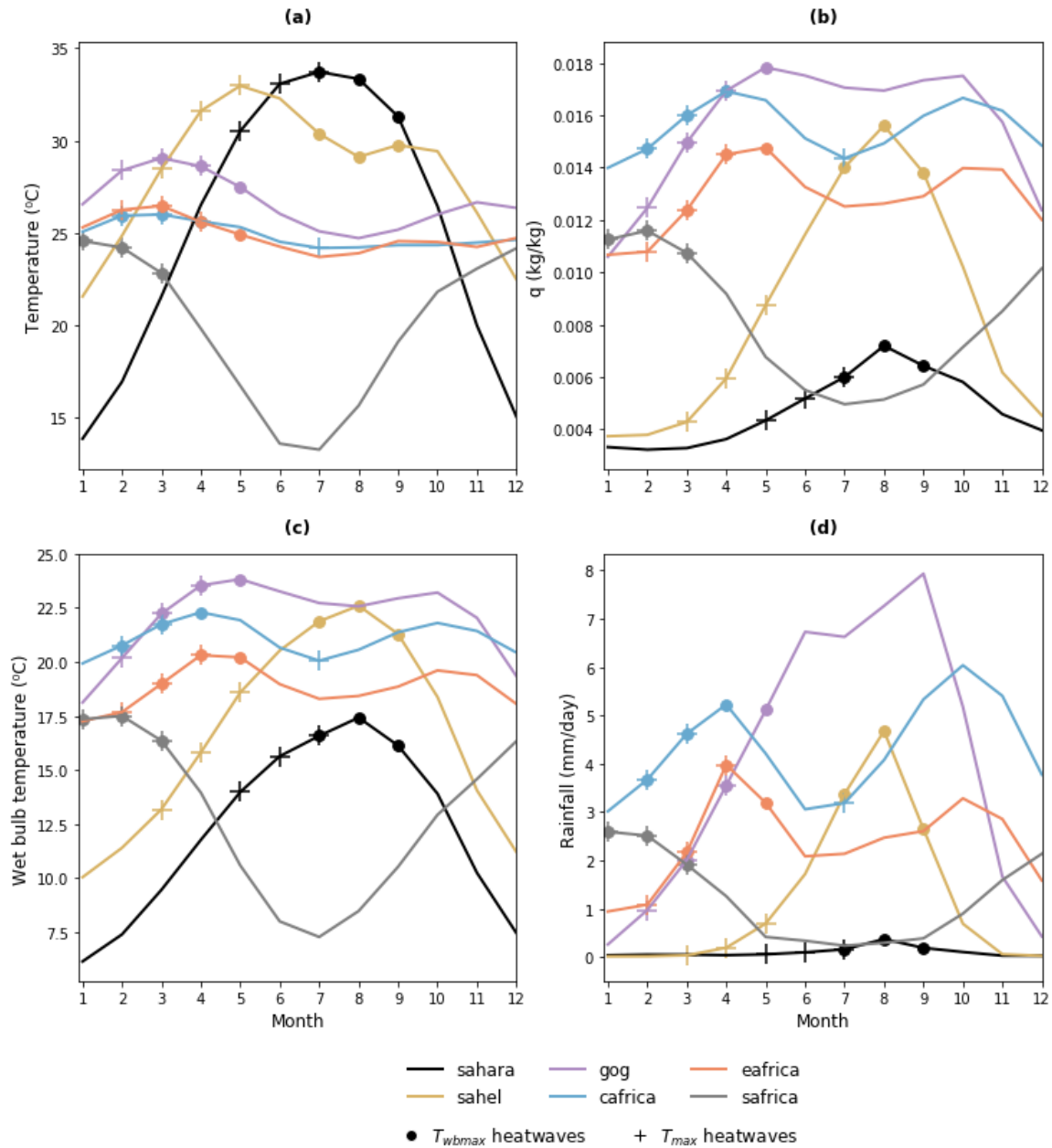
395

396 **Figure 7** Present day and future change in pan-African heatwave metrics in ERA5, P25, CP4
397 (for both T_{wbmax} and T_{max} heatwaves) and BEST (for T_{max} heatwaves only). (a-c) present day
398 T_{wbmax} heatwaves, (d-f) future change in T_{wbmax} heatwaves, (g-i) present day T_{max} heatwaves,
399 (j-l) future change in T_{max} heatwaves. All data is for the period 1997-2006. The numbers in
400 the legends represent the mean and standard error of each distribution. The data in the
401 intensity and duration distributions only includes times and locations where heatwaves were
402 diagnosed and is presented as a frequency of occurrence (i.e. the distribution is divided by
403 the total number of heatwaves diagnosed). The frequency distribution is a count of the
404 number of model grid boxes in each frequency bin.

405

406 **3.3 Drivers of present day wet and dry bulb heatwaves**

407 Figure 8 shows the mean annual cycle of ERA5 near-surface humidity, dry and wet bulb
408 temperature and GPM rainfall for the 6 sub-regions illustrated in Figure 2. T_{max} heatwaves
409 occur most frequently in the months with the highest mean dry bulb temperature, generally
410 before the onset of the rainy season. For example, T_{max} heatwaves occur most frequently in
411 the Gulf of Guinea (GoG) in Feb-Apr before the onset of the monsoon season in May/June. In
412 contrast, T_{wbmax} heatwaves occur most frequently at least a month later, when temperatures
413 are still hot but the humidity is beginning to increase. The difference in the timing of T_{wbmax}
414 and T_{max} heatwaves is largest in the Sahel, where T_{max} heatwaves occur in March-May,
415 consistent with previous studies (Barbier et al. 2018; Guigma et al. 2020; LARGERON et al. 2020),
416 but T_{wbmax} heatwaves occur most frequently in July-Sept, when the mean dry bulb
417 temperature is lower but the mean wet bulb temperature and rainfall is highest.



418

419 **Figure 8** Mean present day annual cycles over the African sub-regions, as defined in Figure
 420 2a. (a) dry-bulb temperature, (b) wet-bulb temperature,(c), specific humidity from ERA5 and
 421 (d) rainfall from GPM. The dots and crosses represent the three months of the year in each
 422 region with the highest occurrence of present day T_{wbmax} and T_{max} heatwaves respectively.

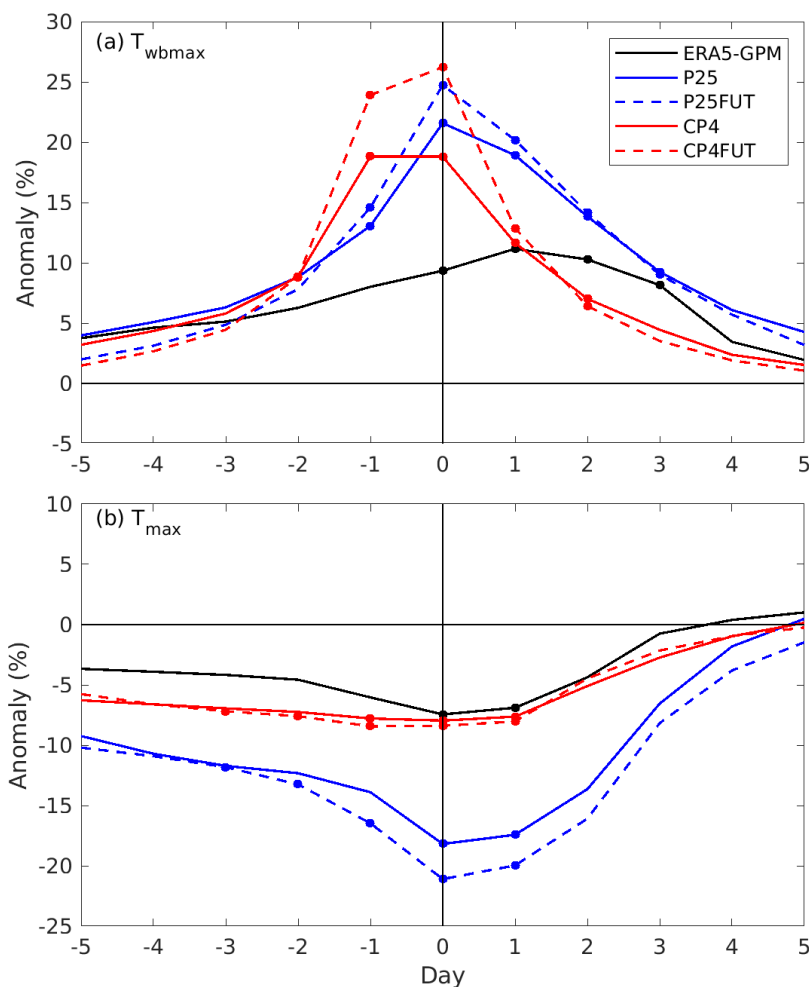
423

424 It is important to understand if rainfall is a driver of and/or a response to humid heatwaves
 425 because it is known that models with parameterised convection struggle to represent rainfall
 426 frequency and intensity (Fiedler et al. 2020) and because there may be a growing risk of
 427 compound heat-flood hazards under climate change (Liao et al. 2021; You; Wang 2021).

428 Figure 9 shows composites of the anomaly of wet day occurrence 5 days before (d-5) to 5
 429 days after (d5) the onset of T_{wbmax} and T_{max} heatwaves, relative to the weighted climatology
 430 of wet day occurrence (see Section 2.5). Wet days are defined as daily rainfall accumulations
 431 of >1 mm. Table 1 shows the percentage of T_{wbmax} and T_{max} heatwaves where the first day of
 432 the heatwave (day 0) is defined as a wet day, compared to the occurrence of wet days in the
 433 weighted climatology.

434

435



436

437 **Figure 9** Composite of wet day (>1 mm/day) occurrence during heatwaves minus wet day
 438 occurrence in the weighted climatology for (a) T_{wbmax} and (b) T_{max} heatwaves over the pan-
 439 African region. Day 0 is the first day of each heatwave. The climatological values take into
 440 account the fact that heatwaves do not occur uniformly in time or space. The climatology is
 441 computed by finding a mean of the frequency of occurrence of wet days in each rainfall
 442 category 15 days before and after each heatwave (d-15 and d15). For ERA5 and the four

443 climate model simulations, when considering the full datasets, the heatwave rainfall
 444 distributions on days -5 to 5 are all statistically significantly different to climatology (Wilcoxon
 445 matched-pairs signed rank test, $p < 0.01$, see Section 2f), which shows that the rainfall
 446 distributions do not come from the same population. The days marked with a dot are when
 447 $>90\%$ of the Wilcoxon tests performed 10,000 times on 1000 randomly selected difference-
 448 pairs have a p value of $p < 0.001$.

	T_{wbmax} (%)		T_{max} (%)	
	1 st day of heatwave	Climatology	1 st day of heatwave	Climatology
ERA5-GPM	32.3	22.9	2.5	11.1
CP4	35.0	16.1	0.8	8.8
CP4FUT	40.3	14.1	0.9	9.3
P25	56.5	34.8	3.0	21.2
P25FUT	58.9	34.1	2.7	23.8

449 **Table 1** Percentage of T_{wbmax} and T_{max} heatwaves associated with wet days (defined as daily
 450 rainfall accumulations of >1 mm). Data is presented for the 1st day of each heatwave and a
 451 climatological value for comparison, which is weighted for the months and locations in which
 452 the heatwaves occur: it is a mean of the rainfall 15 days prior to and 15 days after the 1st day
 453 of each heatwave. For all heatwave-climatology rainfall pairs the Wilcoxon matched-pairs
 454 signed rank test shows that the rainfall distributions do not come from the same population
 455 ($p < 0.01$, see Section 2.6). An expanded version of this table, showing, for each model, the
 456 distribution of rainfall daily accumulations on the 1st day of each heatwave and the difference
 457 between the rainfall climatologies 15 days prior to and after the 1st day of each heatwave is
 458 presented in Table S1.

459
 460 ERA5-GPM and all four climate model simulations show a positive anomaly in wet days
 461 between d-5 and d+5 after the commencement of T_{wbmax} heatwaves (Figure 9a). For all
 462 heatwave-climatology rainfall pairs in Table 1 and Figure 9, the Wilcoxon matched-pairs
 463 signed rank test shows that the rainfall distributions do not come from the same population
 464 ($p < 0.01$, see Section 2.6), so the differences in rainfall on heatwave days and in the
 465 climatology are statistically significant. The dots on Figure 9 show where the anomalies are of
 466 the highest statistical significance (see Figure 9 caption). The wet day anomaly in ERA5-GPM
 467 peaks between d0 and d3 of the heatwaves, whereas the peak in the climate models occurs
 468 the day before the onset of the heatwave (d-1).

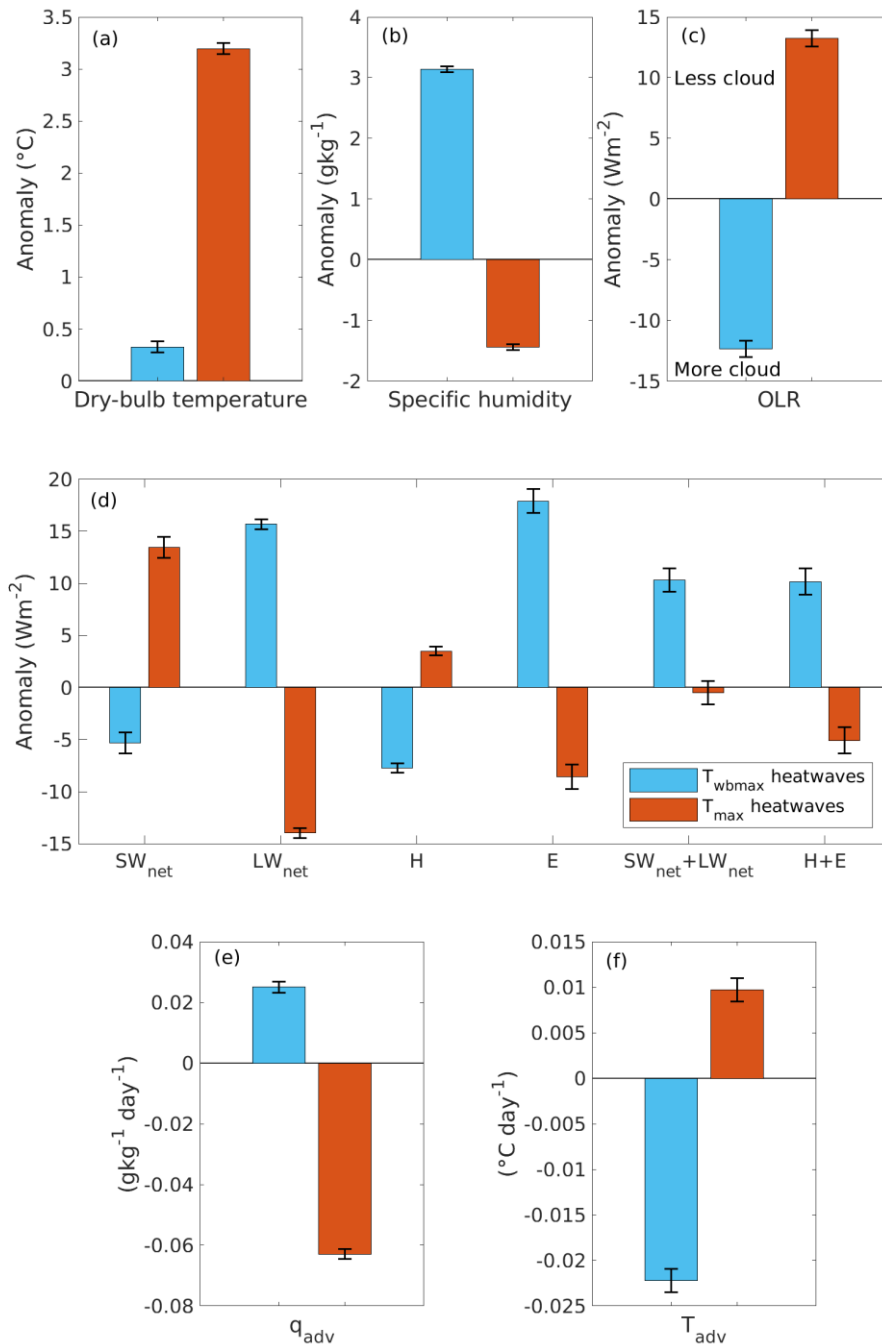
469 It is not clear why there is a difference in the timing of the peak between ERA5-GPM and the
470 models, which means in a pan-African sense at least, it is not clear whether rainfall drives
471 T_{wbmax} heatwaves through evaporation, or the rainfall is a consequence of the increased
472 humidity. However, evaporation from rain that falls during a T_{wbmax} heatwave is likely to help
473 prolong it by maintaining higher levels of near-surface humidity. Splitting the plot into the six
474 sub regions provides more insight (see Section 3.4.2).

475 In ERA5-GPM, T_{wbmax} heatwaves commence on wet days 32.3% of the time compared to an
476 occurrence of wet days 22.9% of the time in climatology i.e wet days occur almost 10% more
477 often on the first day of a T_{wbmax} heatwave than they occur climatologically (Table 1). The
478 pattern in the present day climate models is similar but more extreme, with T_{wbmax} heatwaves
479 commencing on wet days 56.5% of the time in P25 (compared to wet days occurring 34.8% of
480 the time in climatology) and on wet days 35.0% of the time in CP4 (compared to wet days
481 occurring 16.1% of the time in climatology). For both models, T_{wbmax} heatwaves commence
482 about 20% more frequently on wet days than wet days occur in the climatology. The
483 differences in the absolute percentages are due to the known differences in the distribution
484 of rainfall intensity in the convective-scale and parameterised CP4 and P25 models, where
485 parameterised models are known to have more frequent but lower rainfall rates compared
486 to observations (see Table S1 for more detail and (Kendon et al. 2021; Kendon et al. 2014;
487 Prein et al. 2015)). Under climate change, the timing of the peak in wet anomaly stays the
488 same (Figure 9a) but a larger percentage of T_{wbmax} heatwaves commence on wet days (change
489 from 35.0 to 40.3% in CP4 and 56.5 to 58.9% in P25), even though wet days occur
490 approximately the same amount or even slightly less frequently in the climatology of the
491 future simulations (Table 1).

492 The same relationship between present day heatwaves and rainfall is not, however, apparent
493 for T_{max} heatwaves. More than 5 days prior to heatwave onset there is a negative anomaly in
494 wet day occurrence compared to climatology, which peaks at the onset of the heatwave
495 (Figure 9b). By d5 (i.e. after most heatwaves have finished), the wet day occurrence has
496 returned to the climatological value. In ERA5, 2.5% of T_{max} heatwaves commence on wet days,
497 compared to wet days occurring on 11.1% of days climatologically (Table 1). Both CP4 and
498 P25 are in broad agreement with ERA5, in that 0.8% and 3.0% of T_{max} heatwaves respectively
499 commence on wet days, compared to wet days occurring 8.8 and 21.2% of the time

500 respectively in the climatology. There is only a very small change in these percentages with
501 climate change.

502 We now compare the drivers of T_{wbmax} and T_{max} heatwaves in ERA5. Figure 10 shows the mean
503 anomalies of several key variables averaged over the first 3 days of each T_{wbmax} and T_{max}
504 heatwave diagnosed in ERA5, relative to a weighted climatology (see Section 2.5). For T_{wbmax}
505 heatwaves, the anomaly in daily mean dry bulb temperature is relatively small ($+0.32^{\circ}\text{C}$) and
506 there is a large ($+3.2\text{ g/kg}$) anomaly in daily mean specific humidity (blue bars, Figure 10a,b).
507 The anomaly in top of atmosphere Outgoing Longwave Radiation (OLR) is -12 Wm^{-2} , which
508 indicates increased cloud occurs during T_{wbmax} heatwaves compared to climatology. Increased
509 cloud and moisture leads to a decrease in the surface net shortwave radiation flux, SW_{net} , of
510 5 Wm^{-2} and an increase in the surface net longwave radiation flux, LW_{net} , of 15 Wm^{-2} . The
511 sensible heat flux, H , decreases by 8 Wm^{-2} but the latent heat flux, E , increases by 18 Wm^{-2} .
512 The sum of the anomalies of the radiative terms approximately balance the sum of anomalies
513 in the turbulent fluxes, both with a net anomaly of $+10\text{ Wm}^{-2}$ (right hand blue bars, Figure
514 10d). Humidity advection is positive (moistening) but small, at $+0.025\text{ gkg}^{-1}\text{ day}^{-1}$ (Figure 10e)
515 compared to the anomaly in mean humidity of $+3.2\text{ g/kg}$. Temperature advection is negative
516 (cooling) and also small, at $-0.022\text{ }^{\circ}\text{C day}^{-1}$ (Figure 10f), compared to the anomaly in mean
517 temperature of $0.32\text{ }^{\circ}\text{C}$ of the opposite sign.



518

519 **Figure 10** Anomalies relative to climatology of key ERA5 variables over the pan-Africa region
 520 during T_{wbmax} and T_{max} heatwaves diagnosed in ERA5. (a) near-surface daily mean dry bulb
 521 temperature, (b) near-surface daily mean specific humidity, (c) outgoing longwave radiation,
 522 (d) surface net shortwave radiation, longwave radiation, sensible heat flux, latent heat flux
 523 and the sum of the radiative and turbulent terms, (e) 850 hPa moisture advection, (f) 850 hPa
 524 temperature advection. All variables are averaged over the first 3 days of each heatwave. All
 525 variables are presented as anomalies from the climatological annual cycle (see Section 2e),
 526 apart from q_{adv} and T_{adv} , which for ease of interpretation, are the absolute values. The data
 527 for ERA5 are for heatwaves during the period 2001-2019 to align with the availability of GPM
 528 rainfall data plotted in Figure 9. The error bars represent the standard error.

529

530 Conversely, T_{\max} heatwaves occur during much larger daily mean dry bulb temperature
531 anomalies of $+3.2^{\circ}\text{C}$ and dry specific humidity anomalies of -1.4 g/kg , compared to
532 climatology. The OLR anomaly is $+13\text{ Wm}^{-2}$, indicating lower, warmer cloud or a lower cloud
533 fraction compared to climatology. SW_{net} increases by 13 Wm^{-2} and LW_{net} decreases by a
534 similar amount. H increases by 3.5 Wm^{-2} and E decreases by 8.6 Wm^{-2} . Humidity advection is
535 negative (drying) but small, at $-0.063\text{ gkg}^{-1}\text{ day}^{-1}$ (Figure 10e), compared to the anomaly in
536 mean humidity of -1.4 gkg^{-1} (Figure 10b). Temperature advection is positive (warming) but
537 small, at $+0.01\text{ }^{\circ}\text{C day}^{-1}$ (Figure 10f), compared to the positive anomaly in mean temperature
538 of $3.2\text{ }^{\circ}\text{C}$ (Figure 10a).

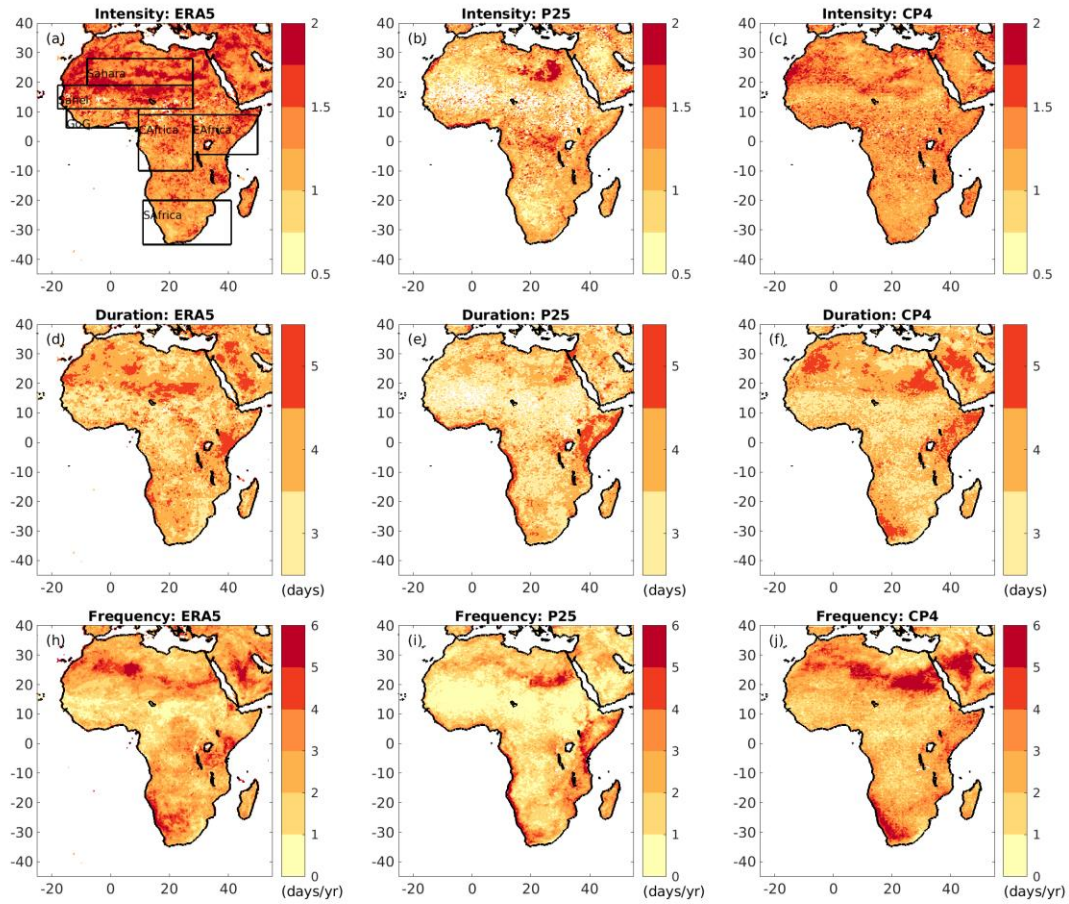
539 In summary, in a pan-African sense, the main driver of T_{wbmax} heatwaves is increased
540 atmospheric moisture, cloud, rainfall and low Bowen ratio (high surface latent heat flux),
541 leading to higher humidity and increased absorption of longwave radiation within the
542 atmospheric column i.e. the water vapour and cloud greenhouse effect. In contrast, T_{\max}
543 heatwaves are driven by decreased cloud cover, increased surface SW_{net} and a high Bowen
544 ratio (high surface sensible heat flux). These results are based on reanalysis, which is itself a
545 model with parameterised convection. It is likely reanalysis is a better representation of dry-
546 bulb heatwaves because they occur at times without cloud and rainfall because moist
547 processes are more challenging to represent in models, especially those with parameterised
548 convection (Fiedler et al. 2020).

549 Given the key role of moist processes in T_{wbmax} heatwaves, their importance for human health
550 (Armstrong et al. 2019), the fact that the model difference between P25 and CP4 in the future
551 change in T_{wbmax} heatwaves is much larger than for T_{\max} heatwaves (Figure 7), and the known
552 differences in the representation of moist processes in convective-scale and convection-
553 parameterised models, the remainder of the paper will focus on T_{wbmax} heatwaves. It will
554 examine the heatwave metrics and drivers on a regional basis and the reasons why the
555 convective-scale climate model projects a larger future change in T_{wbmax} heatwaves.

556 **3.4 Regional analysis of T_{wbmax} heatwaves**

557 **3.4.1 Spatial variability of T_{wbmax} heatwaves**

558 Figure 11 shows maps of the present day T_{wbmax} heatwave metrics in ERA5, P25 and CP4. The
559 white speckling in the intensity and duration plots illustrates regions where no heatwaves are
560 diagnosed in the entire 10 year period. A diagnosis of no heatwaves is possible at locations
561 where there are no occurrences of 3 consecutive hot days. No present day heatwaves were
562 diagnosed in 0.4% of ERA5 gridboxes, 4.4% of P25 gridboxes and 1.0% of CP4 gridboxes.
563 Intensity is fairly uniform to the south of the equator in all three datasets (Figure 11a-c). ERA5
564 produces intensity hotspots in the Sahel and Sahara, whereas there are many gridboxes in
565 P25 over the Sahel where no heatwaves are diagnosed over the 10 year period. CP4 produces
566 a spatial distribution of intensity closer to that in ERA5, with an intensity hotspot between 10
567 and 30°N, although it is not as intense as in ERA5. Hotspots of mean heatwave duration of 5
568 or more days and frequency of 4 or more heatwave days per year are apparent in ERA5 across
569 the Sahel and Sahara, in East Africa and along the southern African west coast (Figure 11d,h).
570 The spatial distribution in CP4 is again closer to the distribution in ERA5 than P25. The hot
571 spot between 10 and 30°N in ERA5 is not apparent in P25, rather it is a region of short duration
572 or no heatwaves (Figure 11e,f,i,j).



573
 574 **Figure 11** Present day T_{wbmax} heatwave metrics. (a-c) intensity, (d-f) duration and (h-j)
 575 frequency for ERA5 (left), P25 (middle) and CP4 (right). The boxes in (a) show the analysed
 576 sub-regions. The white speckled pixels are regions where no heatwaves in 10 years were
 577 diagnosed.

578

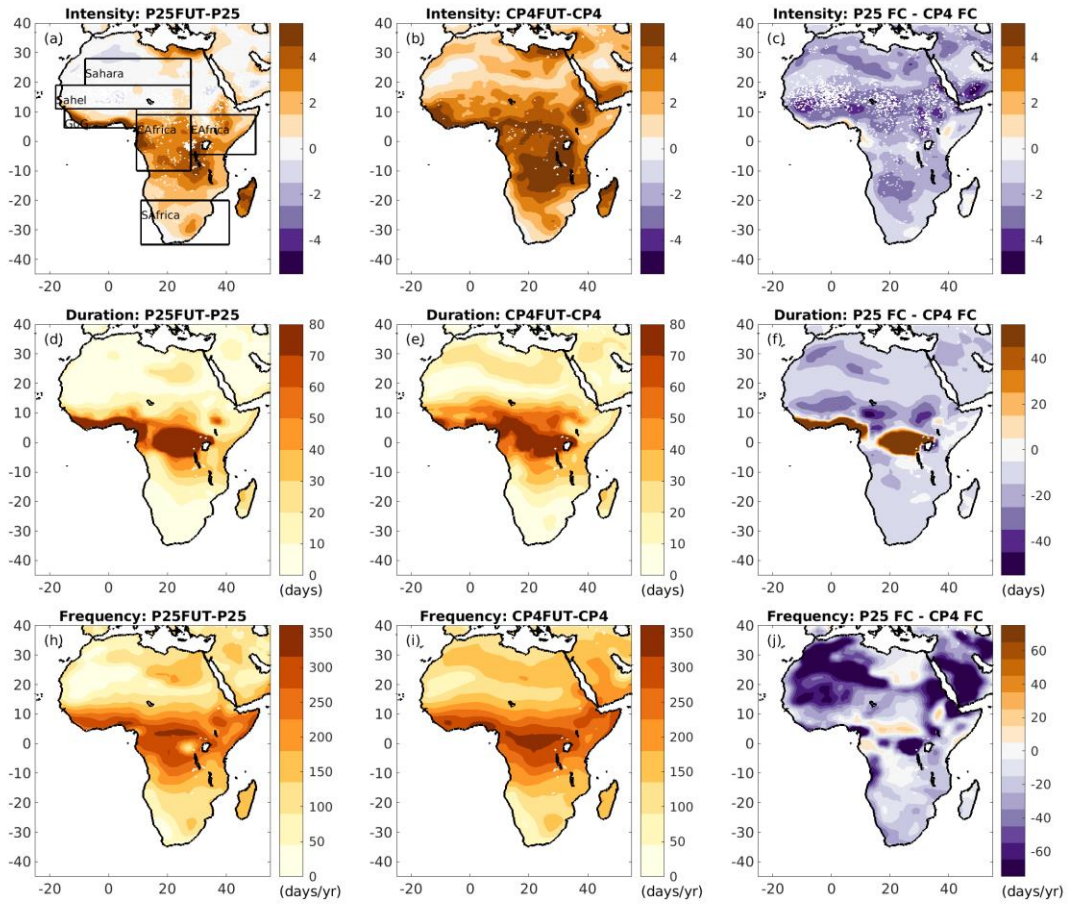
579 Maps of the future change in the three heatwave metrics in P25 and CP4, and the difference
 580 in the future change (P25 future change minus CP4 future change) are shown in Figure 12. In
 581 both climate models there are hot spots in the future change of intensity along the equatorial
 582 belt between 20°S and 5°N, with particularly high values along the GoG coast (Figure 12a,b).
 583 The highest values, of +3 or more, extend across most of sub-Saharan North Africa in CP4.
 584 Overall, the future change in intensity is larger almost everywhere in CP4 than P25 (mean
 585 changes of +3.67 in CP4 compared with +2.35 in P25, Figure 7d), with the largest differences
 586 between the two model simulations 5-15°N and 10-20°S. There are some small patches near
 587 the equator where the change in P25 is greater than in CP4, which are consistent with the
 588 fact that P25 has a greater increase in total column water vapour nearer the equator, linked

589 to model differences in the changing Hadley circulation (Jackson et al. (2020) and Figure 5g
590 showing specific humidity).

591 There is a clear hotspot in the future change in frequency and duration over equatorial Africa
592 (10°S to 10°N) in both P25 and CP4 , which tends to be larger in the more humid West African
593 coast and Central Africa/Congo, rather than the drier East African region. The future change
594 in duration outside this region is up to approximately +20 days, however, within the
595 equatorial belt both models simulate values of greater than +80 days (Figure 12d,e). The
596 future change in duration in CP4 is larger overall compared to that in P25 (+21 and +15 days
597 respectively, Figure 7e). The change is larger north of ~7°N in CP4, whereas the change is
598 larger in P25 over GoG and parts of Central Africa. The measure of duration does, however,
599 break down under climate change as the number of heatwave days per year increases so
600 much therefore, it is better to focus on the intensity and frequency metrics.

601 There is good agreement between CP4 and P25 in the spatial distribution of the future change
602 in frequency, with both models simulating future increases of more than +200 days/yr in the
603 equatorial belt, with largest changes in humid regions, and values of more than +100 days/yr
604 elsewhere (Figure 12h,i). CP4 simulates larger future changes in frequency than P25 (means
605 of +178 days/yr compared to +148 days/yr, Figure 7f) everywhere apart from a small region
606 in Central Africa (Figure 12j), again consistent with the greater total column water vapour
607 increase seen in P25 in this region (Jackson et al. 2020).

608 In summary, the simulations show that by 2100 under RCP8.5, conditions experienced on the
609 present-day wet-bulb heatwave days will be experienced consistently throughout the
610 hottest/wettest three months of the year and over the equatorial belt, these conditions will
611 be experienced up to 50% of the time. The hot spot in the future change in T_{wbmax} heatwave
612 frequency over equatorial Africa is consistent with previous global studies (Coffel et al. 2017;
613 Mora et al. 2017) and is co-located with the area of largest future change in mean humidity,
614 where humidity increases by more than 2 gkg^{-1} (compared to pan-African increases of $<+0.5$
615 gkg^{-1} , Figure 5a,c).



616
 617 **Figure 12** Future change in T_{wbmax} heatwave metrics. (a-c) intensity, (d-f) duration and (h-j)
 618 frequency for P25 (left), CP4 (middle) and the difference in the future change (left minus
 619 middle, right). The boxes in (f) and (j) show the analysed sub-regions.

620

621 3.4.2 T_{wbmax} heatwaves and rainfall

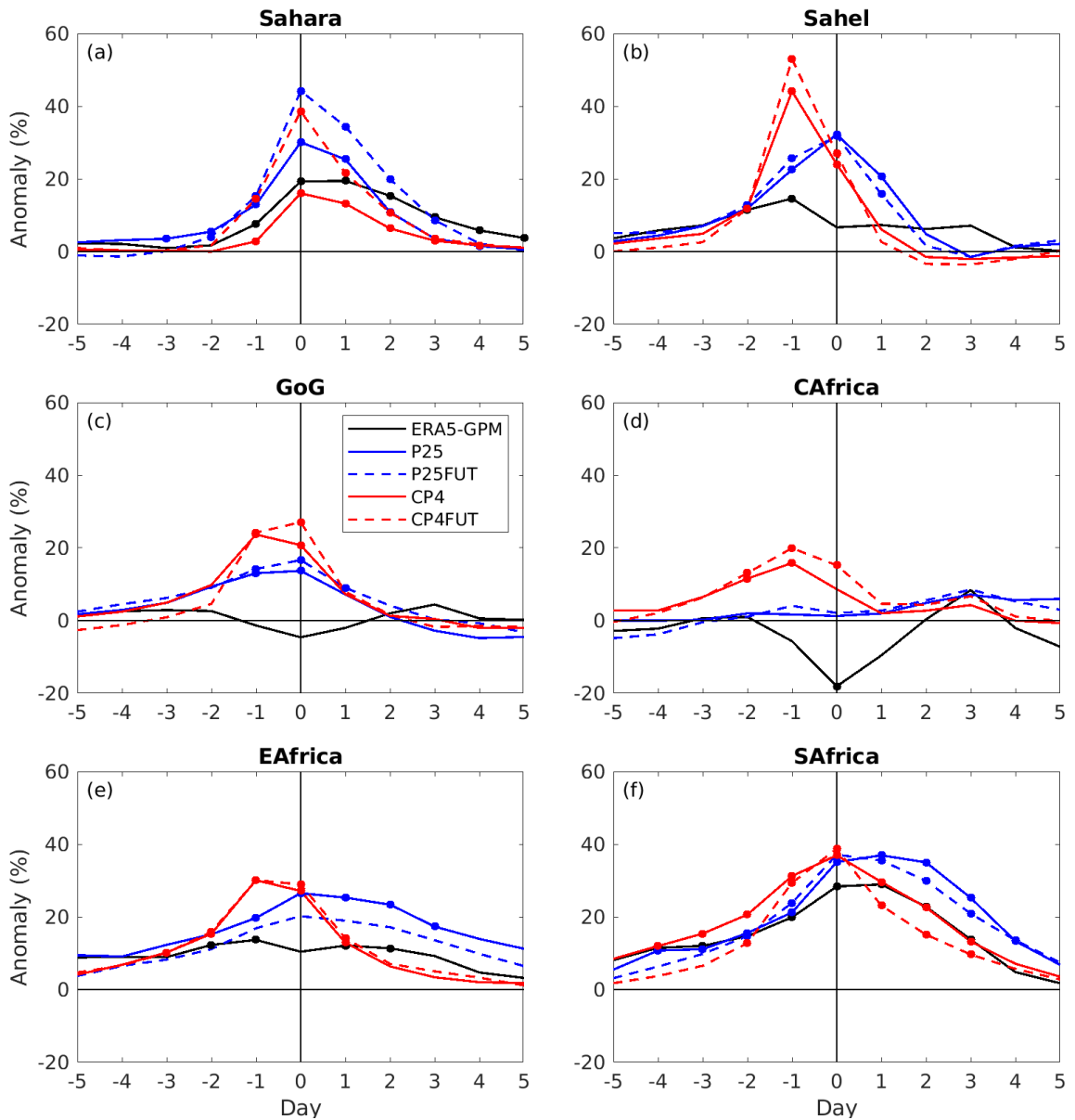
622 Figure 13 shows composites of wet day (>1 mm/day) occurrence relative to climatology
 623 around the time of the onset of T_{wbmax} heatwaves. There are larger, more statistically
 624 significant wet day anomalies over the relatively arid regions of the Sahara, Sahel, EAfrica and
 625 SAfrica. In the Sahara the peak in wet day anomaly coincides with the first day of the T_{wbmax}
 626 heatwave in ERA5-GPM and the four climate model simulations. ERA5-GPM wet days occur
 627 23.6% of the time on the first day of a T_{wbmax} heatwave, compared to wet days occurring 4.3%
 628 of the time in the weighted climatology (the day 0 percentages for all models and regions are
 629 shown in Table S2). In the Sahel, EAfrica and SAfrica the picture is less clear with wet day
 630 anomalies peaking between d-1 and d+1 in ERA5 and the various models. One must
 631 remember here that ERA5-GPM cannot be considered as ‘observations’ or ‘truth’ in this

632 context because ERA5 itself is a parameterised convection model and there may not be full
633 consistency between T_{wbmax} heatwaves diagnosed in ERA5 and the rainfall from GPM.

634 GoG and CAfrica have different behaviour, with smaller positive wet day anomalies in the four
635 climate model simulations and negative anomalies in ERA5-GPM between d-1 and d+1. GoG
636 and CAfrica can be considered as moist equatorial regions, with a lower amplitude annual
637 cycle of humidity and wet bulb temperature and higher mean annual rainfall (Figure 8b-d).
638 Although EAfrica is also within the equatorial belt, it is generally more arid than GoG and
639 CAfrica, with a low amplitude mean annual cycle of humidity but more moderate rainfall.

640 Apart from in the Sahara, the percentage of T_{wbmax} heatwaves associated with wet days
641 decreases or stays almost the same under climate change in all regions and both climate
642 models (Figure 13 and Table S2). Climatologically, the number of wet days decreases in both
643 P25 and CP4 (Table S2). The exceptions are in the Sahara, where wet days increase in both
644 P25 and CP4 and in EAfrica, where they increase in P25. A broad decrease in wet days is
645 consistent with Kendon et al. (2019), who report future increases in dry spell length in the
646 same set of climate model simulations. Since the percentage of climatological wet days and
647 the percentage of heatwaves that occur on wet days both decrease, the overall impact on
648 T_{wbmax} heatwave drivers is minimal. This suggests that the same combination of drivers cause
649 wet-bulb heatwaves in both the present day and under future climate change, and the future
650 increases in wet-bulb heatwaves are driven by larger anomalies in these drivers.

651



652

653 **Figure 13** Composites of wet day (>1 mm/day) occurrence during heatwaves minus wet day
 654 occurrence in the weighted climatology for T_{wbmax} heatwaves only and for each of the 6 sub
 655 regions. Day 0 is the first day of each heatwave. The dots represent the days with the largest
 656 differences between the heatwave and climatological rainfall distributions (see Figure 9
 657 caption for more details). The rainfall climatologies are computed in the same way as in Figure
 658 9.

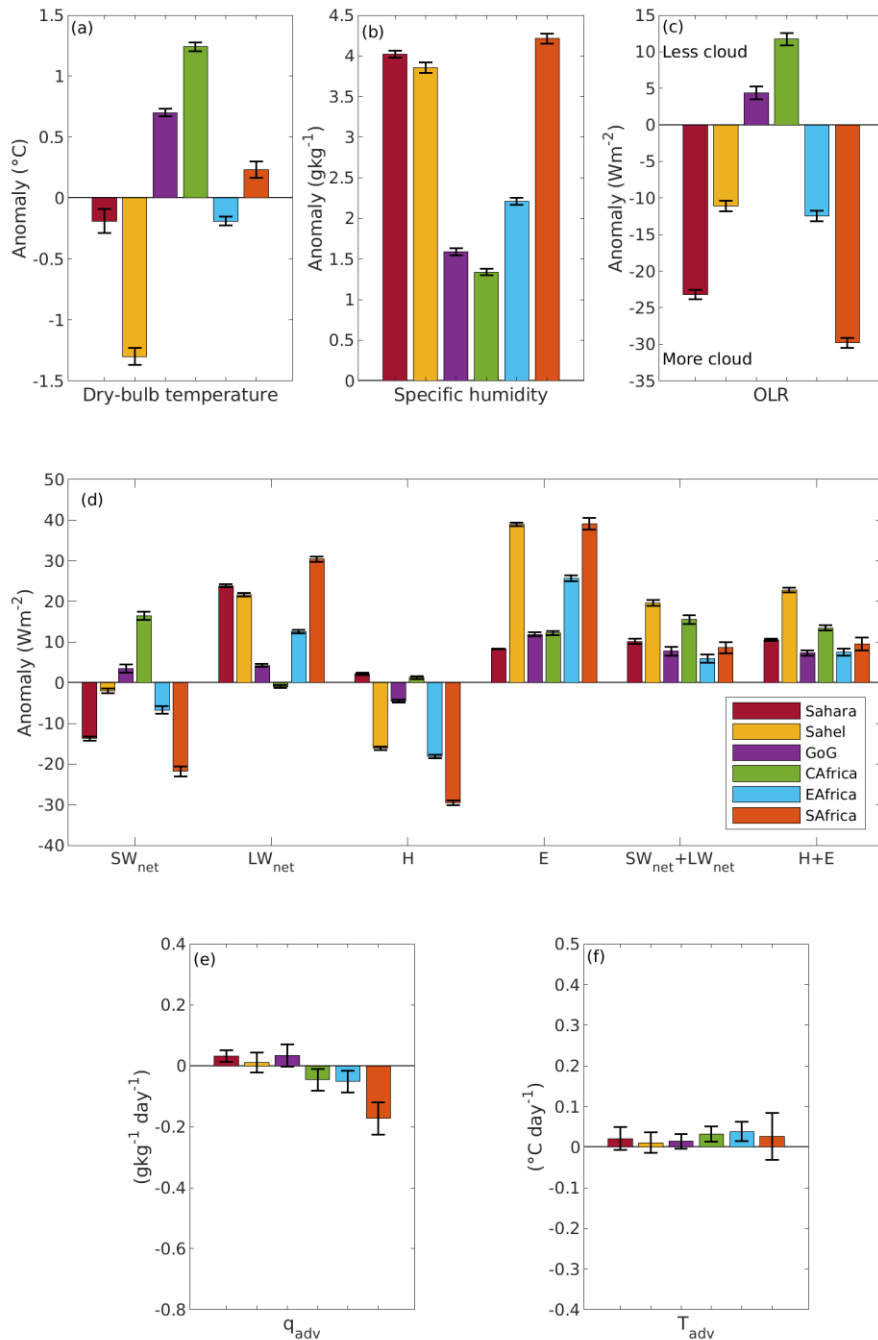
659

660 3.4.3 Drivers of T_{wbmax} heatwaves

661 Figure 14 shows the anomalies of key variables averaged over the first 3 days of each T_{wbmax}
662 heatwave, separately for each sub region and for ERA5 only. Unlike the equivalent plot for
663 T_{max} heatwaves (Figure S2), there are large regional differences in the sign of the anomalies in
664 the T_{wbmax} heatwave plot. The Sahel experiences negative dry bulb temperature anomalies
665 (i.e. cooler than climatology), whereas the equatorial regions of GoG and CAfrica experience
666 positive dry bulb temperature anomalies during T_{wbmax} heatwaves (Figure 14a). Dry bulb
667 temperature anomalies in the other regions are small. There are positive anomalies in specific
668 humidity in all six regions, however, the magnitude is smaller over the already humid GoG
669 and CAfrica. Overall, T_{wbmax} heatwaves are driven by higher values of both dry bulb
670 temperature and humidity in the most humid regions of GoG and CAfrica, but are primarily
671 driven by higher values of humidity elsewhere.

672 Equatorial GoG and CAfrica also behave differently to the other regions in terms of the
673 anomalies in OLR and the surface energy budget terms (Figure 14c). GoG and CAfrica
674 experience small positive anomalies in OLR (i.e. decreased cloud), which leads to positive
675 anomalies in SW_{net} , near-zero anomalies in LW_{net} , near zero anomalies in H and a small
676 positive anomaly in E. Conversely, the other regions experience large negative anomalies in
677 OLR (i.e. increased cloud), which drives negative SW_{net} anomalies, positive LW_{net} anomalies,
678 negative H anomalies and large positive E anomalies. Moisture and temperature advection
679 (shown as absolute values, rather than anomalies for ease of interpretation in Figure 14e,f)
680 are small in all five regions.

681 In summary, the key T_{wbmax} heatwave drivers in the Sahara, Sahel, EAfrica and SAfrica are
682 broadly the same as the pan-African mean in Figure 10, where high humidity, increased cloud,
683 increased rainfall, latent heat flux and longwave warming in the atmospheric column are
684 important. In the equatorial regions of GoG and CAfrica, where humidity is climatologically
685 the highest, T_{wbmax} heatwaves are driven by a mixture of high temperature and humidity, with
686 decreased cloud and increased shortwave warming.



687

688 **Figure 14** Anomalies relative to climatology of key ERA5 variables by sub-region during
 689 present day ERA5 T_{wbmax} heatwaves. (a) near-surface daily mean dry bulb temperature, (b)
 690 near-surface daily mean specific humidity, (c) outgoing longwave radiation, (d) surface net
 691 shortwave radiation, longwave radiation, sensible heat flux, latent heat flux and the sum of
 692 the radiative and turbulent terms, (e) 850 hPa moisture advection, (f) 850 hPa temperature
 693 advection. All variables are averaged over the first 3 days of each heatwave. All variables are
 694 presented as anomalies from the climatological annual cycle (see Section 2.5), apart from q_{adv}
 695 and T_{adv} , which for ease of interpretation, are the absolute values. The data for ERA5 are for
 696 heatwaves during the period 2001-2019 to align with the availability of the GPM rainfall data
 697 plotted in Figure 13. The error bars represent the standard error.

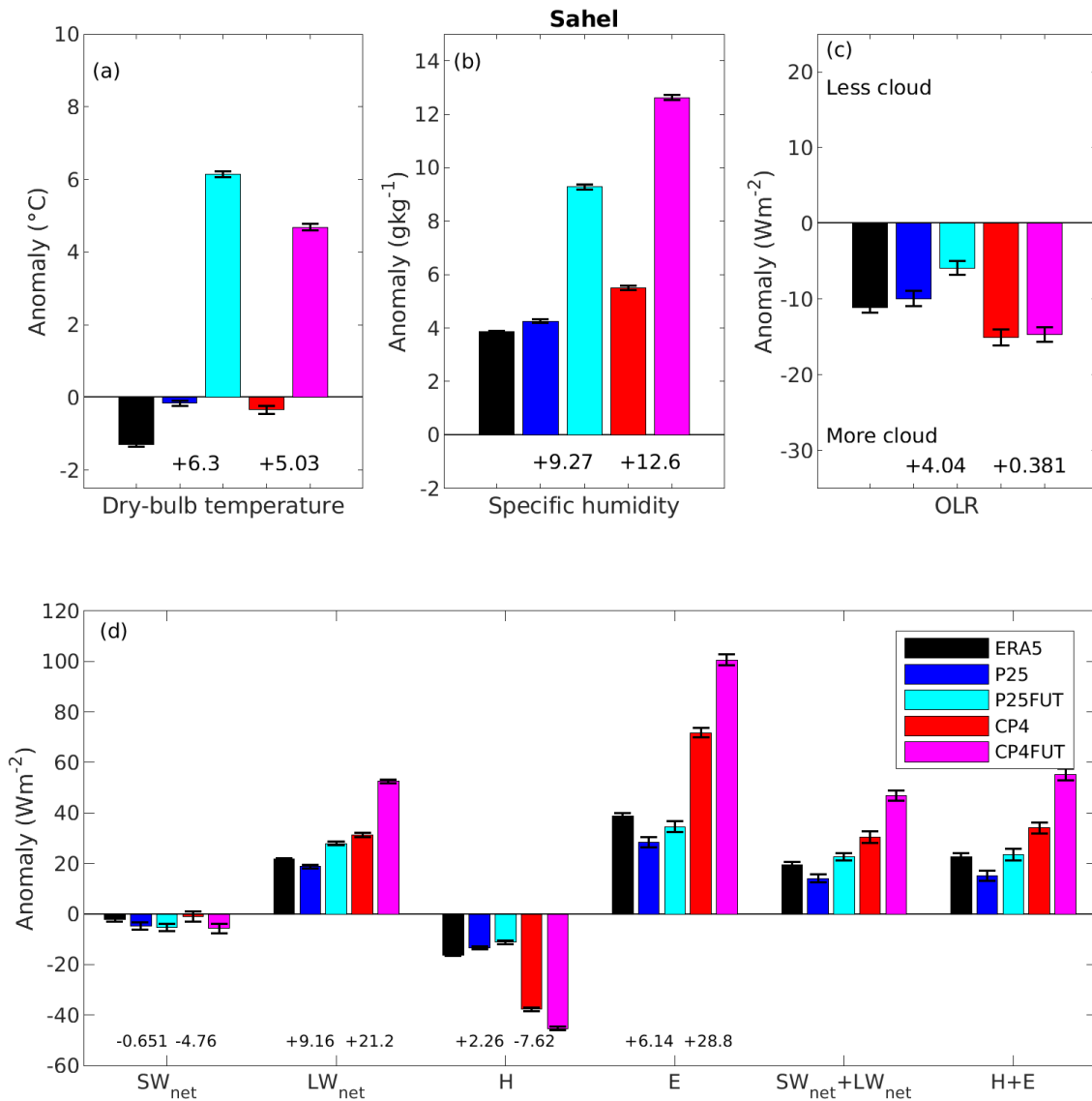
698 **3.4.4 Future change in heatwave drivers**

699 Now we examine the future change in T_{wbmax} heatwave drivers in P25 and CP4 in order to
700 understand why CP4 simulates a larger future change in T_{wbmax} heatwaves over almost all
701 parts of Africa. We examine two regions: the Sahel, a region outside of the equatorial belt,
702 where CP4 simulates a much larger future change in heatwave intensity and frequency than
703 P25 (Figure 15) and CAfrica, a region within the equatorial belt (i.e. within the future change
704 'hotspot'), where the simulated future change in P25 and CP4 is more similar (Figure 16). Plots
705 of the other regions are shown in Figures S3-5, where GoG behaves broadly like CAfrica and
706 the Sahara, SAfrica and EAfrica behave broadly like the Sahel. In Figures 15 and 16, the future
707 T_{wbmax} heatwaves are diagnosed using a future climate (rather than present day) baseline (see
708 Section 2.3) and the anomalies are relative to present day climatology.

709 In the Sahel, the dry bulb temperature during T_{wbmax} heatwaves relative to present day
710 climatology increases by 6.3°C and 5.0°C in P25 and CP4 respectively under climate change
711 (Figure 15a). The specific humidity anomaly also increases in both models but to a larger
712 extent in CP4 (9.3 g/kg in P25 compared to 12.6 g/kg in CP4. Figure 15b). Cloud during T_{wbmax}
713 heatwaves decreases slightly in the future in both P25 and CP4, i.e. the heatwaves occur over
714 slightly less cloudy skies (Figure 15c). The main difference between P25 and CP4 is the
715 increase in LW_{net} warming and the increase in latent heat flux (Figure 15d). The future increase
716 in LW_{net} warming is 9.2 Wm^{-2} in P25 and 21.2 Wm^{-2} in CP4 and the future increase in latent
717 heat flux is 6.1 Wm^{-2} in P25 and 28.8 Wm^{-2} in CP4, both of these increases are much larger in
718 CP4 than P25. For the present day anomalies, P25 is generally in better agreement with ERA5
719 than CP4. However, given ERA5 is also produced from a model with parameterised
720 convection, in a region with limited in-situ observations, it is not possible to determine
721 whether P25 or CP4 is a better representation of reality.

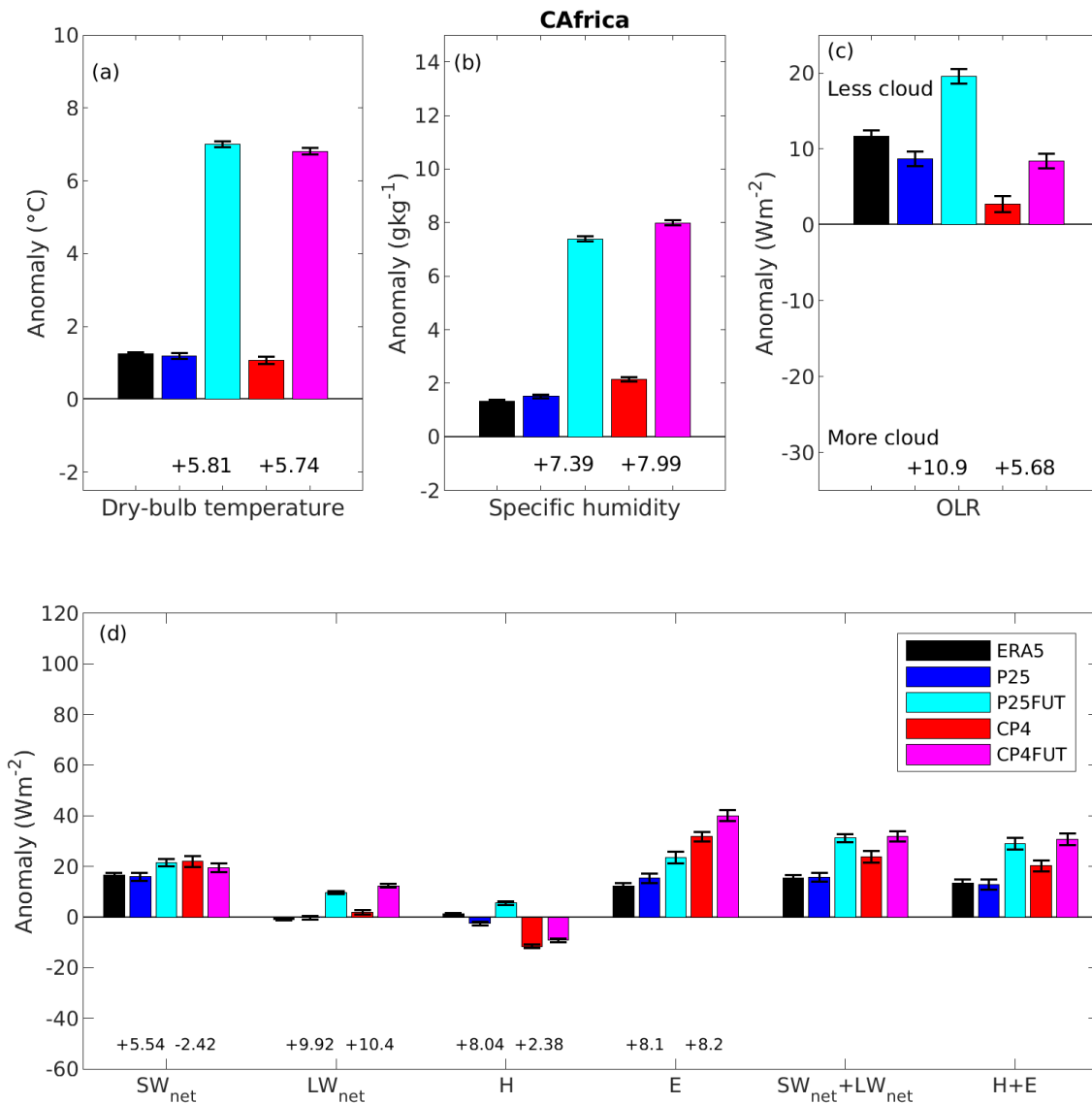
722 In CAfrica, the future increases in the dry bulb temperature and specific humidity anomalies
723 are similar in P25 and CP4 and are of the order +5-6°C and +7-8 g/kg respectively (Figure
724 16a,b). Cloud cover becomes even less prevalent during T_{wbmax} heatwaves in the future, i.e.
725 the heatwaves occur over clearer skies, and this change is larger in P25 (+10.9 Wm^{-2}) than CP4
726 (+5.68 Wm^{-2}). The P25-CP4 difference in the future change in the anomalies in Figure 16d is
727 much smaller in CAfrica than the Sahel. For example the future change in LW_{net} anomaly is
728 +9.2 Wm^{-2} and +10.4 Wm^{-2} for P25 and CP4 respectively in CAfrica, compared to +9.1 Wm^{-2}

729 and $+21.1 \text{ Wm}^{-2}$ in the Sahel. This is also the case for the latent heat flux, where the values in
 730 CAfrica are $+8.1$ and $+8.2 \text{ Wm}^{-2}$ for P25 and CP4 respectively, compared to $+6.1$ and $+28.8$
 731 Wm^{-2} in the Sahel.



732

733 **Figure 15** Mean anomalies of key variables averaged over the first 3 days of each T_{wbmax}
 734 heatwave over the Sahel, relative to a representative mean annual cycle (see Section 2.5) for
 735 ERA5 and the four climate model simulations. The bars for P25FUT and CP4FUT represent
 736 heatwaves diagnosed using the future climate baseline (see Section 2.3) and are anomalies
 737 from the present day annual cycle. The numbers under the P25 and CP4 present day/future
 738 climate bar pairs show the future change in the anomaly of each variable. For example, in (a)
 739 the future change in the dry bulb temperature anomaly is $+6.3^\circ\text{C}$ in P25 and $+5.03^\circ\text{C}$ in CP4.
 740 The error bars represent the standard error.



741

742 **Figure 16** Same as Figure 15 but for CAfrica.

743

744 **4 Discussion and conclusions**

745 The present day and future wet and dry bulb heatwaves are assessed in 10 year convective-
 746 scale (CP4, 4.5km) and parameterised convection (P25, 25km) simulations over the entire
 747 African continent. Compared to reanalysis, CP4 better reproduces the intensity and frequency
 748 of wet bulb heatwaves (and their spatial distribution) than P25. For dry bulb heatwaves, the
 749 difference between the two climate model simulations is much smaller, with both in good
 750 agreement with reanalysis and observations.

751 Both CP4 and P25 show large increases in the intensity, duration and frequency of dry (T_{\max})
752 and wet bulb (T_{wbmax}) heatwaves by 2100 under RCP8.5. Present day conditions that occur on
753 3 to 6 heatwave days per year are expected to be normal by 2100, occurring on 150-180 days
754 per year. Huge future increases such as this are consistent with previous global and regional
755 studies (Coffel et al. 2017; Mora et al. 2017; Russo et al. 2017).

756 P25 and CP4 simulate similar future changes in T_{\max} heatwaves, however, the future change
757 in T_{wbmax} heatwaves is larger in CP4 than P25: future changes in intensity are +3.67 compared
758 to +2.35 and future changes in frequency are +178 days/yr compared to +148 days/yr. The
759 difference in the future change between the two model simulations occurs despite very
760 similar future increases in the mean specific humidity and dry bulb temperature. Both CP4
761 and P25 have a cold and dry bias in their mean climate, which is common for climate models
762 in the tropics (Zhao et al. 2015). These biases in the mean climate will cause absolute values
763 of wet bulb temperature to be biased too low, which is not an issue for the percentile-based
764 heatwave metric used in this study, but is an issue for measures of humid heatwaves that use
765 absolute thresholds, such as the survivability threshold of 35°C in wet bulb temperature,
766 where sweating becomes ineffective (Sherwood; Huber 2010). Bias correction may not be
767 possible due to the lack of routine humidity observations over Africa.

768 This study uses reanalysis to document the differences in the present day drivers of T_{\max} and
769 T_{wbmax} heatwaves over the entire African continent. The timing of T_{\max} and T_{wbmax} heatwave
770 events within the annual cycle is different. T_{\max} heatwaves occur in the warm and dry pre-
771 monsoon months, such as March-May in the Sahel, consistent with previous literature
772 (Barbier et al. 2018; Fontaine et al. 2013; Guigma et al. 2020), whereas T_{wbmax} heatwaves tend
773 to occur at the start and/or during the rainy season (July-Sept in the Sahel), when
774 temperatures remain reasonably high but humidity increases.

775 African T_{\max} heatwaves are associated with low rainfall (only 2.5% of T_{\max} heatwaves
776 commence on wet days), decreased humidity and cloud, higher shortwave surface warming,
777 and a high sensible heat flux. This is in broad agreement with Bouniol et al. (2021) and Hong
778 et al. (2018), who both found similar drivers from observations for T_{\max} heatwaves over the
779 Sahel and Korean Peninsula respectively. In contrast, African T_{wbmax} heatwaves are associated
780 with much larger humidity anomalies than dry bulb temperature anomalies. They are
781 associated with rainfall, increased cloud and humidity, increased evaporation and increased

782 longwave warming within the atmospheric column i.e. the greenhouse warming effect. In
783 ERA5, 32% of T_{wbmax} heatwaves commence on wet days, compared to wet days occurring 23%
784 of the time in a weighted climatology. Through the process of evaporation, soil moisture could
785 be a key driver of African humid heatwaves during the wet season and should be a focus of
786 future research. In a pan-African sense, moisture and temperature advection appear to play
787 only a limited role in both types of heatwaves.

788 The T_{wbmax} heatwave drivers documented here, which are associated with moist processes,
789 are similar to those diagnosed by Bouniol et al. (2021) for daily minimum dry bulb
790 temperature (T_{min}) heatwaves. Given both T_{min} and T_{wbmax} heatwaves are associated with
791 increases in humidity, it is possible that the differences between P25 and CP4 for T_{min}
792 heatwaves would be the similar to those documented here for T_{wbmax} heatwaves. Bouniol et
793 al. (2021) also found reduced and increased aerosol load during T_{max} and T_{min} heatwaves
794 respectively. Dust and aerosol are not considered in this study, but their impact on T_{wbmax}
795 heatwaves should be explored in future work.

796 Both P25 and CP4 simulate a hot spot of large future change in T_{wbmax} heatwaves over the
797 equatorial regions of Africa, consistent with previous research on humid heatwaves (Coffel et
798 al. 2017; Mora et al. 2017). This hotspot is co-located with a large future increase in mean
799 specific humidity over the equator in both models. This study, for the first time, compares the
800 drivers of present day T_{wbmax} heatwaves over different regions of Africa. Outside the
801 equatorial belt, the drivers of T_{wbmax} heatwaves are similar to the pan-African mean described
802 above. The equatorial belt is climatologically moister and experiences higher rainfall than
803 elsewhere. In contrast to elsewhere, T_{wbmax} heatwaves are driven by both temperature and
804 humidity anomalies (rather than predominantly by humidity). The heatwaves occur under
805 increased shortwave surface heating at the same time as increased evaporation from rainfall.
806 Large regional variations in the drivers of African humid heatwaves (relative to the more
807 consistent drivers of T_{max} heatwaves) is consistent with the findings of Raymond et al. (2021)
808 who studies a number of different regions around the world.

809 The results from this study highlight the potential for an increase in co-occurring or
810 consecutive events (“compound hazards”) of African heatwaves, heavy rainfall and flooding,
811 as has been observed in other regions such as China and the USA (Liao et al. 2021;
812 Raghavendra et al. 2019; You; Wang 2021). Both P25 and CP4 simulate future increases in the

813 percentage of T_{wbmax} heatwaves that occur on days with >10 mm daily rainfall accumulations.
814 In CP4 this increase extends to days with >50 mm daily rainfall accumulations (Table S1).
815 Humid heat events occurring at the same time as heavy rainfall and flooding could potentially
816 overwhelm road, hospital and power infrastructure and lead to a higher number of fatalities
817 and economic damage than if these events occurred in isolation (Zhang; Villarini 2020).

818 T_{wbmax} heatwaves are driven by moist processes. The fundamental difference between CP4
819 and P25 model configurations is the representation of convection, so the reason for the larger
820 future change in humid heatwaves in CP4 must originate from its representation of moist
821 processes. CP4 simulates larger anomalies than P25 in almost all the key T_{wbmax} heatwave
822 drivers (temperature, humidity, cloud, rainfall, radiation, turbulent fluxes) in the future
823 compared to the present day. This is true in all the sub regions apart from equatorial regions
824 of Central Africa and the Gulf of Guinea, where the difference in the future change in T_{wbmax}
825 heatwaves in P25 and CP4 is much smaller. Previous studies show that convective-scale
826 climate models are better able to represent extremes and respond realistically to
827 environmental controls, giving a greater intensification of rainfall under climate change (Ban
828 et al. 2020; Birch et al. 2014a; Chan et al. 2016; Finney et al. 2020; Finney et al. 2019;
829 Fitzpatrick et al. 2020b; Jackson et al. 2020; Prein et al. 2015).

830 Climate models with parameterised convection, such as those used in the Coupled Model
831 Intercomparison Project (CMIP), have similar issues with moist processes as P25 (Fiedler et al.
832 2020), so they may also underestimate the future change in humid heatwaves. This heightens
833 the need for mitigation and adaptation strategies and also indicates that, if anything, there is
834 even less time available to implement such changes to avoid catastrophic future heat
835 conditions than previously thought.

836 The analysis in this study has highlighted that it is critical to account for the fact that the mean
837 diurnal cycle of humidity is out of phase with the mean diurnal cycle of dry bulb temperature:
838 specific humidity peaks overnight but dry bulb temperature peaks during the day. Previous
839 studies using CMIP5 models (Coffel et al. 2017; Russo et al. 2017), for example, necessarily
840 use daily mean specific humidity to convert daily maximum dry bulb temperature to daily
841 maximum wet bulb temperature, because sub daily diagnostics are generally unavailable.
842 Analysis in this study shows the values of daily maximum wet bulb temperature and the
843 subsequent heatwave diagnostics that are computed can be very sensitive to the choice of

844 humidity averaging period. Climate model simulations that are run in the future should, if
845 practical, output hourly temperature and humidity data, or implement the computation of
846 heat stress metrics within the model simulation, as recommended by Buzan et al. (2015).

847 **Acknowledgements**

848 This work was funded by the Department for International Development/Natural
849 Environment Research Council via the Future Climate for Africa (FCFA) funded project
850 Improving Model Processes for African Climate (IMPALA, NE/M017214/1 and
851 NE/MO17176/1) and U.K. Research and Innovation as part of the Global Challenges Research
852 Fund, (GCRF African SWIFT, NE/P021077/1). Marsham and Finney were also funded via the
853 FCFA HyCRISTAL (NE/M019985/1) project and Marsham by AMMA-2050 (NE/M019977/1).
854 Kendon gratefully acknowledges funding from the Joint U.K. BEIS/Defra Met Office Hadley
855 Centre Climate Programme (GA01101). Keane was supported by the Centre for
856 Environmental Computation and Modelling (CEMAC), University of Leeds. Birch and Chapman
857 were also supported through the Global Challenges Research Fund, AFRICAP programme,
858 Grant Number BB/P027784/1. We are grateful for the use of the Centre for Environmental
859 Data Analysis (CEDA)-Jasmin computing facilities, ERA5 data from the Copernicus Climate
860 Change Service (C3S) Climate Data Store, GPM-IMERG data from Goddard Earth Sciences Data
861 and Information Services Centre, temperature observations from Berkeley Earth and the
862 Climatic Research Unit, and weather station observations from Niger through AMMA-CATCH,
863 from South Africa through FLUXNET and from the station in Central Sudan.

864

865 **Data Availability Statement**

866 A subset of the CP4 and P25 climate model data used in this study is freely available from the
867 Centre for Environmental Data Analysis at
868 <https://catalogue.ceda.ac.uk/uuid/a6114f2319b34a58964dfa5305652fc6>, IMPALA:
869 Improving model processes for African climate, as cited in (Senior 2019a, 2019b, 2019c,
870 2019d). The full dataset is also freely available, but due its size, contact the lead author of this
871 paper for access. Daily maximum temperature observations used in this study are openly
872 available from the Berkeley Earth Surface Temperature gridded dataset at
873 <http://berkeleyearth.org/data/> as cited in Rohde; Hausfather (2020). The monthly mean
874 temperature observations used in this study are openly available from the Climatic Research
875 Unit at <https://crudata.uea.ac.uk/cru/data/hrg/> as cited in Harris et al. (2020). The weather
876 station data from Demokeya, Kordofan, central Sudan is freely available from
877 <https://www.hindawi.com/journals/dpis/2013/297973/dataset/> as cited in Ardö (2013), the
878 data from Banizoumbou, Niamey, Niger is freely available from AMMA-CATCH at
879 <http://bd.amma-catch.org/> as cited in Lebel et al. (2009) and the data from Skukuza, South
880 Africa is available from <https://fluxnet.org/>. The daily satellite rainfall retrievals used in this
881 study are freely available from Goddard Earth Sciences Data and Information Services Centre
882 at https://disc.gsfc.nasa.gov/datasets/GPM_3IMERGDF_06/summary, as cited in Huffman
883 (2014). The ERA5 reanalysis data is also freely available from the Copernicus Climate Change
884 Service (C3S) Climate Data Store at DOI: 10.24381/cds.adbb2d47 and DOI:
885 10.24381/cds.bd0915c6 as cited in Hersbach et al. (2020).

886 **References**

- 887 Ardö, J., 2013: A 10-Year Dataset of Basic Meteorology and Soil Properties in Central Sudan. *Dataset*
888 *Papers in Geosciences*, **2013**, 297973.
- 889 Armstrong, B., and Coauthors, 2019: The Role of Humidity in Associations of High Temperature with
890 Mortality: A Multicountry, Multicity Study. *Environmental Health Perspectives*, **127**, 097007.
- 891 Azongo, D. K., T. Awine, G. Wak, F. N. Binka, and A. Rexford Oduro, 2012: A time series analysis of
892 weather variables and all-cause mortality in the Kasena-Nankana Districts of Northern Ghana, 1995–
893 2010. *Global Health Action*, **5**, 19073.
- 894 Ban, N., J. Rajczak, J. Schmidli, and C. Schär, 2020: Analysis of Alpine precipitation extremes using
895 generalized extreme value theory in convection-resolving climate simulations. *Climate Dynamics*, **55**,
896 61-75.
- 897 Barbier, J., F. Guichard, D. Bouniol, F. Couvreur, and R. Roehrig, 2018: Detection of Intraseasonal
898 Large-Scale Heat Waves: Characteristics and Historical Trends during the Sahelian Spring. *Journal of*
899 *Climate*, **31**, 61-80.
- 900 Berthou, S., E. J. Kendon, D. P. Rowell, M. J. Roberts, S. Tucker, and R. A. Stratton, 2019a: Larger
901 Future Intensification of Rainfall in the West African Sahel in a Convection-Permitting Model.
902 *Geophysical Research Letters*, **46**, 13299-13307.
- 903 Berthou, S., D. P. Rowell, E. J. Kendon, M. J. Roberts, R. A. Stratton, J. A. Crook, and C. Wilcox, 2019b:
904 Improved climatological precipitation characteristics over West Africa at convection-permitting
905 scales. *Climate Dynamics*, **53**, 1991-2011.
- 906 Birch, C. E., J. H. Marsham, D. J. Parker, and C. M. Taylor, 2014a: The scale dependence and structure
907 of convergence fields preceding the initiation of deep convection, **41**, 4769-4776.
- 908 Birch, C. E., D. J. Parker, J. H. Marsham, D. Copsey, and L. Garcia-Carreras, 2014b: A seamless
909 assessment of the role of convection in the water cycle of the West African Monsoon. *Journal of*
910 *Geophysical Research*, **119**, 2890-2912.
- 911 Bouniol, D., F. Guichard, J. Barbier, F. Couvreur, and R. Roehrig, 2021: Sahelian Heat Wave
912 Characterization From Observational Data Sets, **126**, e2020JD034465.
- 913 Buzan, J. R., K. Oleson, and M. Huber, 2015: Implementation and comparison of a suite of heat stress
914 metrics within the Community Land Model version 4.5. *Geosci. Model Dev.*, **8**, 151-170.
- 915 Ceccherini, G., S. Russo, I. Amezttoy, A. F. Marchese, and C. Carmona-Moreno, 2017: Heat waves in
916 Africa 1981–2015, observations and reanalysis. *Nat. Hazards Earth Syst. Sci.*, **17**, 115-125.
- 917 Chan, S. C., E. J. Kendon, N. M. Roberts, H. J. Fowler, and S. Blenkinsop, 2016: Downturn in scaling of
918 UK extreme rainfall with temperature for future hottest days. *Nature Geoscience*, **9**, 24-28.
- 919 Coffel, E. D., R. M. Horton, and A. de Sherbinin, 2017: Temperature and humidity based projections
920 of a rapid rise in global heat stress exposure during the 21st century. *Environmental Research*
921 *Letters*, **13**, 014001.
- 922 Couvreur, F., and Coauthors, 2015: Representation of daytime moist convection over the semi-arid
923 Tropics by parametrizations used in climate and meteorological models, **141**, 2220-2236.
- 924 Crook, J., C. Klein, S. Folwell, C. M. Taylor, D. J. Parker, R. Stratton, and T. Stein, 2019: Assessment of
925 the Representation of West African Storm Lifecycles in Convection-Permitting Simulations, **6**, 818-
926 835.
- 927 Davies-Jones, R., 2008: An Efficient and Accurate Method for Computing the Wet-Bulb Temperature
928 along Pseudoadiabats. *Monthly Weather Review*, **136**, 2764-2785.
- 929 Diboulo, E., A. Sié, J. Rocklöv, L. Niamba, M. Yé, C. Bagagnan, and R. Sauerborn, 2012: Weather and
930 mortality: a 10 year retrospective analysis of the Nouna Health and Demographic Surveillance
931 System, Burkina Faso. *Global Health Action*, **5**, 19078.
- 932 Dosio, A., 2017: Projection of temperature and heat waves for Africa with an ensemble of CORDEX
933 Regional Climate Models. *Climate Dynamics*, **49**, 493-519.
- 934 Dosio, A., L. Mentaschi, E. M. Fischer, and K. Wyser, 2018: Extreme heat waves under 1.5 °C and 2 °C
935 global warming. *Environmental Research Letters*, **13**, 054006.

936 Eyring, V., S. Bony, G. A. Meehl, C. A. Senior, B. Stevens, R. J. Stouffer, and K. E. Taylor, 2016:
937 Overview of the Coupled Model Intercomparison Project Phase 6 (CMIP6) experimental design and
938 organization. *Geosci. Model Dev.*, **9**, 1937-1958.

939 Fiedler, S., and Coauthors, 2020: Simulated Tropical Precipitation Assessed across Three Major
940 Phases of the Coupled Model Intercomparison Project (CMIP). *Monthly Weather Review*, **148**, 3653-
941 3680.

942 Finney, D. L., J. H. Marsham, D. P. Rowell, E. J. Kendon, S. O. Tucker, R. A. Stratton, and L. S. Jackson,
943 2020: Effects of Explicit Convection on Future Projections of Mesoscale Circulations, Rainfall, and
944 Rainfall Extremes over Eastern Africa. *Journal of Climate*, **33**, 2701-2718.

945 Finney, D. L., and Coauthors, 2019: Implications of Improved Representation of Convection for the
946 East Africa Water Budget Using a Convection-Permitting Model. *Journal of Climate*, **32**, 2109-2129.

947 Fischer, E. M., and R. Knutti, 2013: Robust projections of combined humidity and temperature
948 extremes. *Nature Climate Change*, **3**, 126-130.

949 Fitzpatrick, R. G. J., and Coauthors, 2020a: How a typical West African day in the future-climate
950 compares with current-climate conditions in a convection-permitting and parameterised convection
951 climate model. *Climatic Change*, **163**, 267-296.

952 Fitzpatrick, R. G. J., and Coauthors, 2020b: What Drives the Intensification of Mesoscale Convective
953 Systems over the West African Sahel under Climate Change? *Journal of Climate*, **33**, 3151-3172.

954 Fontaine, B., S. Janicot, and P.-A. Monerie, 2013: Recent changes in air temperature, heat waves
955 occurrences, and atmospheric circulation in Northern Africa. *Journal of Geophysical Research*, **118**,
956 8536-8552.

957 Gregory, D., and P. R. Rowntree, 1990: A Mass Flux Convection Scheme with Representation of Cloud
958 Ensemble Characteristics and Stability-Dependent Closure. *Monthly Weather Review*, **118**, 1483-
959 1506.

960 Guigma, K. H., M. Todd, and Y. Wang, 2020: Characteristics and thermodynamics of Sahelian
961 heatwaves analysed using various thermal indices. *Climate Dynamics*, **55**, 3151-3175.

962 Guigma, K. H., F. Guichard, M. Todd, P. Peyrille, and Y. Wang, 2021: Atmospheric tropical modes are
963 important drivers of Sahelian springtime heatwaves. *Climate Dynamics*, **56**, 1967-1987.

964 Gutowski Jr, W. J., and Coauthors, 2016: WCRP COordinated Regional Downscaling EXperiment
965 (CORDEX): a diagnostic MIP for CMIP6. *Geosci. Model Dev.*, **9**, 4087-4095.

966 Harrington, L. J., and F. E. L. Otto, 2020: Reconciling theory with the reality of African heatwaves.
967 *Nature Climate Change*, **10**, 796-798.

968 Harris, I., T. J. Osborn, P. Jones, and D. Lister, 2020: Version 4 of the CRU TS monthly high-resolution
969 gridded multivariate climate dataset. *Scientific Data*, **7**, 109.

970 Hart, N. C. G., R. Washington, and R. A. Stratton, 2018: Stronger Local Overturning in Convective-
971 Permitting Regional Climate Model Improves Simulation of the Subtropical Annual Cycle, **45**, 11,334-
972 311,342.

973 Hersbach, H., and Coauthors, 2020: The ERA5 global reanalysis. *Quarterly Journal of the Royal
974 Meteorological Society*, **146**, 1999-2049.

975 Hong, J.-S., S.-W. Yeh, and K.-H. Seo, 2018: Diagnosing Physical Mechanisms Leading to Pure Heat
976 Waves Versus Pure Tropical Nights Over the Korean Peninsula, **123**, 7149-7160.

977 Huffman, G., D. Bolvin, D. Braithwaite, K. Hsu, R. Joyce, P. Xie, 2014: Integrated Multi-satellitE
978 Retrievals for GPM (IMERG), version 6, NASA's Precipitation Processing Center, accessed 23 June
979 2020, <ftp://arthurhou.pps.eosdis.nasa.gov/gpmdata/>.

980 Im, E.-S., J. S. Pal, and E. A. B. Eltahir, 2017: Deadly heat waves projected in the densely populated
981 agricultural regions of South Asia. *Science Advances*, **3**, e1603322.

982 Jackson, L. S., and Coauthors, 2020: The Effect of Explicit Convection on Couplings between Rainfall,
983 Humidity, and Ascent over Africa under Climate Change. *Journal of Climate*, **33**, 8315-8337.

984 Kendon, E. J., A. F. Prein, C. A. Senior, and A. Stirling, 2021: Challenges and outlook for convection-
985 permitting climate modelling, **379**, 20190547.

986 Kendon, E. J., N. M. Roberts, H. J. Fowler, M. J. Roberts, S. C. Chan, and C. A. Senior, 2014: Heavier
987 summer downpours with climate change revealed by weather forecast resolution model. *Nature*
988 *Climate Change*, **4**, 570-576.

989 Kendon, E. J., R. A. Stratton, S. Tucker, J. H. Marsham, S. Berthou, D. P. Rowell, and C. A. Senior,
990 2019: Enhanced future changes in wet and dry extremes over Africa at convection-permitting scale.
991 *Nature Communications*, **10**, 1794.

992 Kennedy-Asser, A. T., O. Andrews, D. M. Mitchell, and R. F. Warren, 2020: Evaluating heat extremes
993 in the UK Climate Projections (UKCP18). *Environmental Research Letters*, **16**.

994 Kjellstrom, T., D. Briggs, C. Freyberg, B. Lemke, M. Otto, and O. Hyatt, 2016: Heat, Human
995 Performance, and Occupational Health: A Key Issue for the Assessment of Global Climate Change
996 Impacts, **37**, 97-112.

997 Largeron, Y., F. Guichard, R. Roehrig, F. Couvreur, and J. Barbier, 2020: The April 2010 North African
998 heatwave: when the water vapor greenhouse effect drives nighttime temperatures. *Climate*
999 *Dynamics*, **54**, 3879-3905.

1000 Lebel, T., and Coauthors, 2009: AMMA-CATCH studies in the Sahelian region of West-Africa: An
1001 overview. *Journal of Hydrology*, **375**, 3-13.

1002 Liao, Z., Y. Chen, W. Li, and P. Zhai, 2021: Growing Threats From Unprecedented Sequential Flood-
1003 Hot Extremes Across China, **48**, e2021GL094505.

1004 Lyon, B., 2009: Southern Africa Summer Drought and Heat Waves: Observations and Coupled Model
1005 Behavior. *Journal of Climate*, **22**, 6033-6046.

1006 Mora, C., and Coauthors, 2017: Global risk of deadly heat. *Nature Climate Change*, **7**, 501-506.

1007 Moron, V., B. Oueslati, B. Pohl, S. Rome, and S. Janicot, 2016: Trends of mean temperatures and
1008 warm extremes in northern tropical Africa (1961–2014) from observed and PPCA-reconstructed time
1009 series. *Journal of Geophysical Research*, **121**, 5298-5319.

1010 Moss, R. H., and Coauthors, 2010: The next generation of scenarios for climate change research and
1011 assessment. *Nature*, **463**, 747-756.

1012 Oueslati, B., B. Pohl, V. Moron, S. Rome, and S. Janicot, 2017: Characterization of Heat Waves in the
1013 Sahel and Associated Physical Mechanisms. *Journal of Climate*, **30**, 3095-3115.

1014 Pal, J. S., and E. A. B. Eltahir, 2016: Future temperature in southwest Asia projected to exceed a
1015 threshold for human adaptability. *Nature Climate Change*, **6**, 197-200.

1016 Pastorello, G., and Coauthors, 2020: The FLUXNET2015 dataset and the ONEFlux processing pipeline
1017 for eddy covariance data. *Scientific Data*, **7**, 225.

1018 Perkins-Kirkpatrick, S. E., and S. C. Lewis, 2020: Increasing trends in regional heatwaves. *Nature*
1019 *Communications*, **11**, 3357.

1020 Prein, A. F., and Coauthors, 2015: A review on regional convection-permitting climate modeling:
1021 Demonstrations, prospects, and challenges. *Reviews of Geophysics*, **53**, 323-361.

1022 Raghavendra, A., A. Dai, S. M. Milrad, and S. R. Cloutier-Bisbee, 2019: Floridian heatwaves and
1023 extreme precipitation: future climate projections. *Climate Dynamics*, **52**, 495-508.

1024 Raymond, C., and Coauthors, 2021: On the Controlling Factors for Globally Extreme Humid Heat, **48**,
1025 e2021GL096082.

1026 Reynolds, R. W., T. M. Smith, C. Liu, D. B. Chelton, K. S. Casey, and M. G. Schlax, 2007: Daily High-
1027 Resolution-Blended Analyses for Sea Surface Temperature. *Journal of Climate*, **20**, 5473-5496.

1028 Rohde, R. A., and Z. Hausfather, 2020: The Berkeley Earth Land/Ocean Temperature Record. *Earth*
1029 *Syst. Sci. Data*, **12**, 3469-3479.

1030 Russo, S., J. Sillmann, and E. M. Fischer, 2015: Top ten European heatwaves since 1950 and their
1031 occurrence in the coming decades. *Environmental Research Letters*, **10**.

1032 Russo, S., J. Sillmann, and A. Sterl, 2017: Humid heat waves at different warming levels. *Scientific*
1033 *Reports*, **7**, 7477.

1034 Russo, S., A. Marchese, S. J., and G. Immé, 2016: When will unusual heat waves become normal in a
1035 warming Africa? *Environmental Research Letters*, **11**.

1036 Seneviratne et al. , S. I., X. Zhang, M. Adnan, W. Badi, C. Dereczynski, A. Di Luca, S. Ghosh, I. Iskandar,
1037 J. Kossin, S. Lewis, F. Otto, I. Pinto, M. Satoh, S.M. Vicente-Serrano, M. Wehner, and B. Zhou,, 2021:
1038 Weather and Climate Extreme Events in a Changing Climate. In *Climate Change 2021: The Physical*
1039 *Science Basis. Contribution of Working Group I to the Sixth Assessment Report of the*
1040 *Intergovernmental Panel on Climate Change.* [Masson-Delmotte, V., P. Zhai, A. Pirani, S.L. Connors,
1041 C. Péan, S. Berger, N. Caud, Y. Chen, L. Goldfarb, M.I. Gomis, M. Huang, K. Leitzell, E. Lonnoy, J. B. R.
1042 Matthews, T. K. Maycock, T. Waterfield, O. Yelekçi, R. Yu, and B. Zhou (eds.)]. Cambridge University
1043 Press. In Press. .
1044 Senior, C. A., 2019a: P25-Present: Present-day 25km regional pan-Africa data. Centre for
1045 Environmental Data Analysis,
1046 <https://catalogue.ceda.ac.uk/uuid/4e362effa16146abbe45c2c58f1e54ed>.
1047 —, 2019b: CP4A-Present: Present-day climate predictions for Africa, Centre for Environmental
1048 Data Analysis, <https://catalogue.ceda.ac.uk/uuid/f46b14e670fc49cbaadf108c969e7ee0>.
1049 —, 2019c: P25-Future: Future 25km regional pan-Africa data. Centre for Environmental Data
1050 Analysis, <https://catalogue.ceda.ac.uk/uuid/8f8eab18b07e420a9b7230d86ed172fe>.
1051 —, 2019d: CP4A-Future: Future climate predictions for Africa. Centre for Environmental Data
1052 Analysis, <https://catalogue.ceda.ac.uk/uuid/a027093520b2432b8e782e3edefd6b47>.
1053 Senior, C. A., and Coauthors, 2021: Convection permitting regional climate change simulations for
1054 understanding future climate and informing decision making in Africa. *Bulletin of the American*
1055 *Meteorological Society*, 1-46.
1056 Sherwood, S. C., 2018: How Important Is Humidity in Heat Stress? *Journal of Geophysical Research*,
1057 **123**, 11,808-811,810.
1058 Sherwood, S. C., and M. Huber, 2010: An adaptability limit to climate change due to heat stress.
1059 *Proceedings of the National Academy of Sciences*, **107**, 9552.
1060 Stratton, R. A., and Coauthors, 2018: A Pan-African Convection-Permitting Regional Climate
1061 Simulation with the Met Office Unified Model: CP4-Africa. *Journal of Climate*, **31**, 3485-3508.
1062 Taylor, C. M., C. E. Birch, D. J. Parker, N. Dixon, F. Guichard, G. Nikulin, and G. M. S. Lister, 2013:
1063 Modeling soil moisture-precipitation feedback in the Sahel: Importance of spatial scale versus
1064 convective parameterization. *Geophysical Research Letters*, **40**, 6213-6218.
1065 Taylor, K. E., R. J. Stouffer, and G. A. Meehl, 2012: An Overview of CMIP5 and the Experiment Design.
1066 *Bulletin of the American Meteorological Society*, **93**, 485-498.
1067 Tölle, M. H., L. Schefczyk, and O. Gutjahr, 2018: Scale dependency of regional climate modeling of
1068 current and future climate extremes in Germany. *Theoretical and Applied Climatology*, **134**, 829-848.
1069 Vicedo-Cabrera, A. M., and Coauthors, 2021: The burden of heat-related mortality attributable to
1070 recent human-induced climate change. *Nature Climate Change*, **11**, 492-500.
1071 Walters, D., and Coauthors, 2017: The Met Office Unified Model Global Atmosphere 6.0/6.1 and
1072 JULES Global Land 6.0/6.1 configurations. *Geosci. Model Dev.*, **10**, 1487-1520.
1073 You, J., and S. Wang, 2021: Higher Probability of Occurrence of Hotter and Shorter Heat Waves
1074 Followed by Heavy Rainfall, **48**, e2021GL094831.
1075 Zhang, W., and G. Villarini, 2020: Deadly Compound Heat Stress-Flooding Hazard Across the Central
1076 United States, **47**, e2020GL089185.
1077 Zhao, Y., A. Ducharne, B. Sultan, P. Braconnot, and R. Vautard, 2015: Estimating heat stress from
1078 climate-based indicators: present-day biases and future spreads in the CMIP5 global climate model
1079 ensemble. *Environmental Research Letters*, **10**.

1080